The two central-ignition head cases showed improvement in ISFC when SOI changed from more homogeneous cases (SOI >100 degrees BTDC) to more stratified cases, around 70 degrees BTDC. In this range of SOI, with less mixing time, average 0-10% burn duration decreased. For all engine configurations, the 0-10% burn durations exhibited minima, where decreasing EOI led to increased 0-10% burn duration.

The two dual-side-ignition heads showed different performance. The dual-side-ignition head with the 5H injector, benefiting from two spark plugs, reduced 0-10% burn by 6 degrees at SOI > 180 degrees when compared to the central injection head. The burn duration improved as SOI decreased and mixing times decreased, until SOI reached 40 degrees. The 3+3H injector had a maximum 10-90% burn rate at SOI = 115 degrees BTDC, which corresponded to the highest fuel consumption for that hardware. From an SOI of 70 degrees BTDC, progressively later injection timing resulted in progressively shorter time required for 0-10% burn. Presumably, this performance was due to progressively richer mixtures close to the spark plugs, a hypothesis that was examined in more detail with optical engine measurements.

Although a correlation between burn rate and thermal efficiency might be expected, Figures 6.5 and 6.6 show that this correlation is not always entirely straightforward. Figure 6.5 shows ITE plotted against 0-10% burn duration. When the single-central-ignition cylinder head was used, efficiency improved, in general, when 0-10% burn duration decreased. However, when the dual-side-ignition cylinder head was used, the correlation was much less direct.

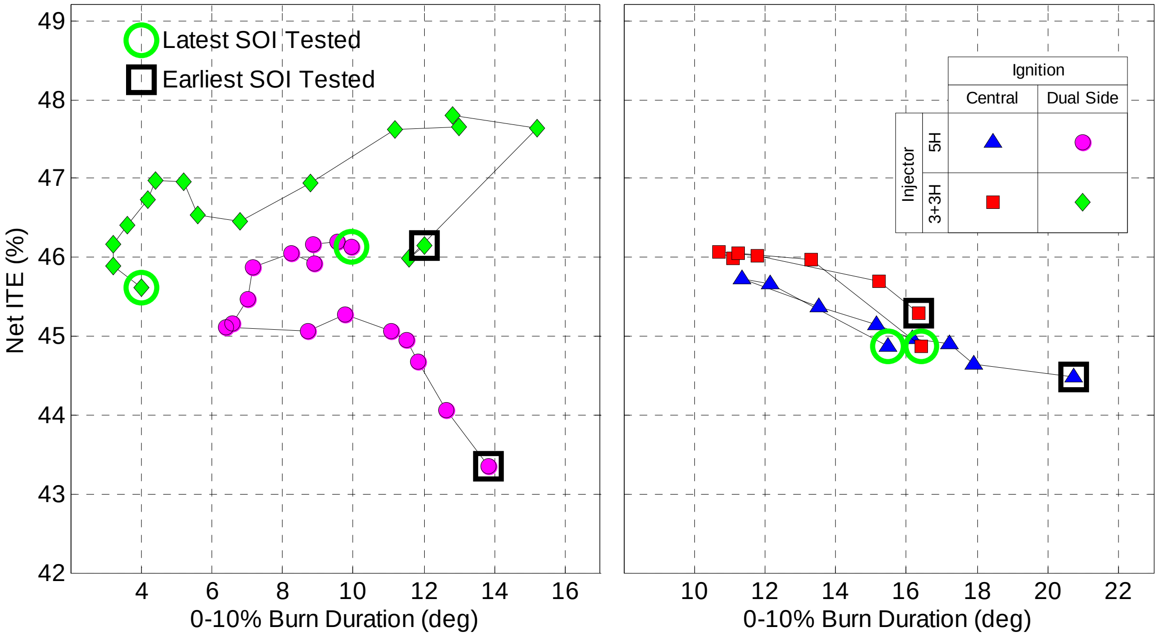

Figure 6.5: Correlation between 0-10% burn rate and efficiency; dual-side-ignition cylinder head (left) and single-central-ignition cylinder head (right).

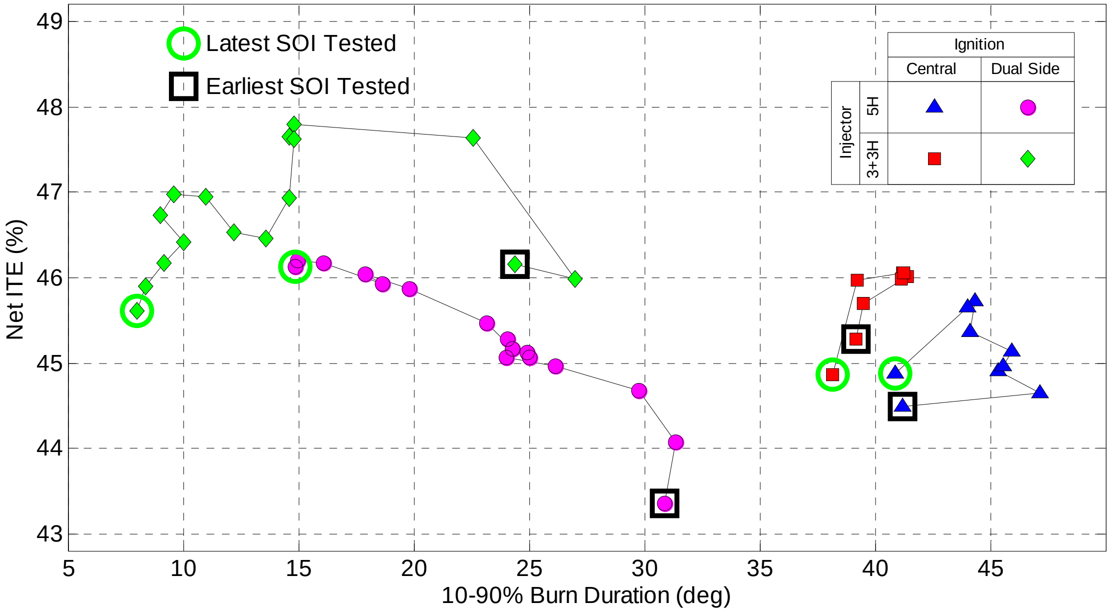

Figure 6.6: Correlation between 10-90% burn rate and efficiency.

In Figure 6.6, net ITE is shown as a function of 10-90% burn duration. The correlation between 10-90% burn duration and efficiency is not straightforward in three of the four cases shown, the lone exception being the 5H injector when paired with the dual-side-ignition cylinder head.

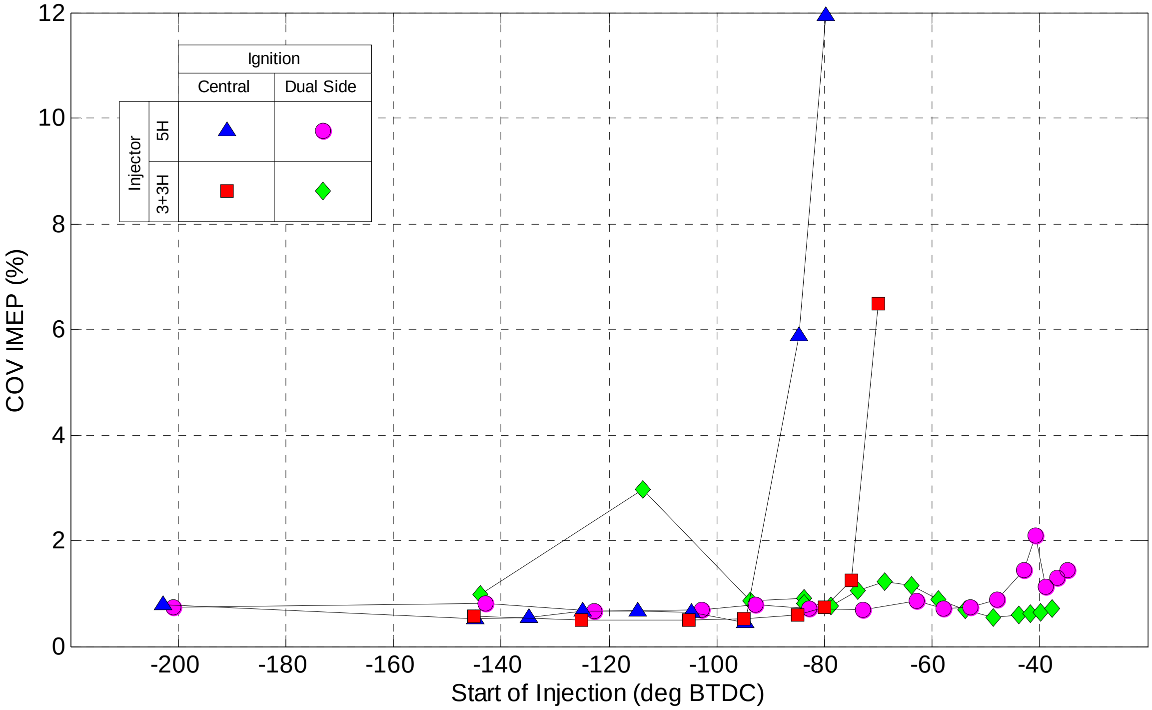

Figure 6.7: Combustion stability as a function of injection timing.

Combustion stability measured as the coefficient of variation (COV) of IMEP is shown in Figure 6.7. For the central ignition cylinder head, stability performed as expected, with stable combustion (COV values <~5) observed with longer mixing periods/early SOI. The dual-side-ignition cylinder head exhibited different modes of performance. The baseline 5H injector showed stable performance even at very late injection timings with the dual side ignition head. The 3+3 injector showed some combustion instabilities at SOI = 110 degrees, with more stable combustion seen with both earlier and later injection timings with the dual side ignition head.

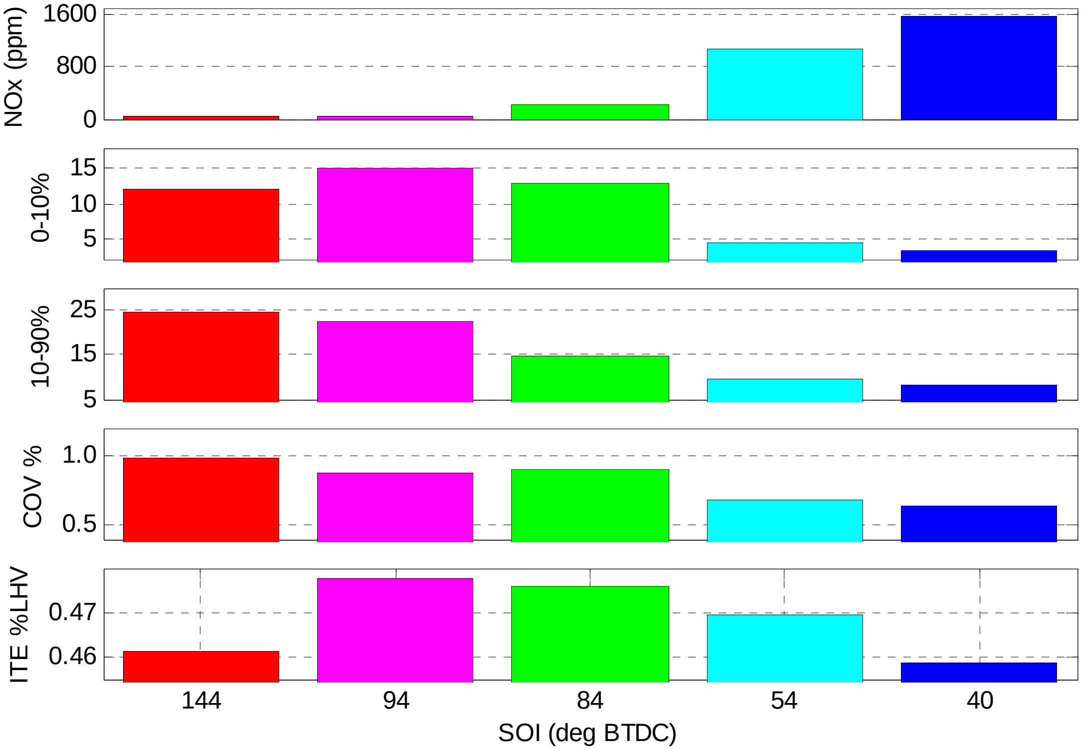

Figure 6.8: Summary of combustion statistics and NO_x production for five injection timings for the 3+3H injector with dual-side-ignition cylinder head.

In summary, during the conditions tested a wide range of burn rates, combustion stabilities, NO_x production, and other performance metrics were observed. The correlation between combustion statistics and resultant engine efficiency was not always as expected. Figure 6.8 shows some of this disparity, plotting burn duration, NO_x production, combustion stability, and thermal efficiency for five pertinent operating conditions for the 3+3H/dual side ignition cylinder head. The shortest burn durations and most stable combustion do not correspond to the best efficiency. At SOI timings of 54 and 40 degrees, the NO_x production is high, indicating high in-cylinder temperatures, and suggesting that the majority of the fuel is burned in zones of the cylinder where the mixture is significantly stratified fuel-rich. High temperatures also suggest that heat transfer to the cylinder wall could have a significant impact on fuel efficiency, and further analysis is warranted.

Figures 6.9-6.11 show some of the high-speed pressure data taken for the results shown in Figure 6.8. The data are shown for five injection timings, corresponding to the conditions shown in Figure 6.8. Figure 6.9 shows pressure as a function of crank angle. The same pressure information is plotted as a function of cylinder volume in Figure 6.10. Significant burn rate changes can be seen, suggesting combustion is highly stratified as injection timing approaches TDC. At the longest mixing times/earliest injection timing of SOI = 144, the peak pressure is significantly reduced compared to the less advanced SOIs. At the shortest mixing times/latest injection timing of SOI = 20, ignition is retarded several degrees later than the other SOI conditions.

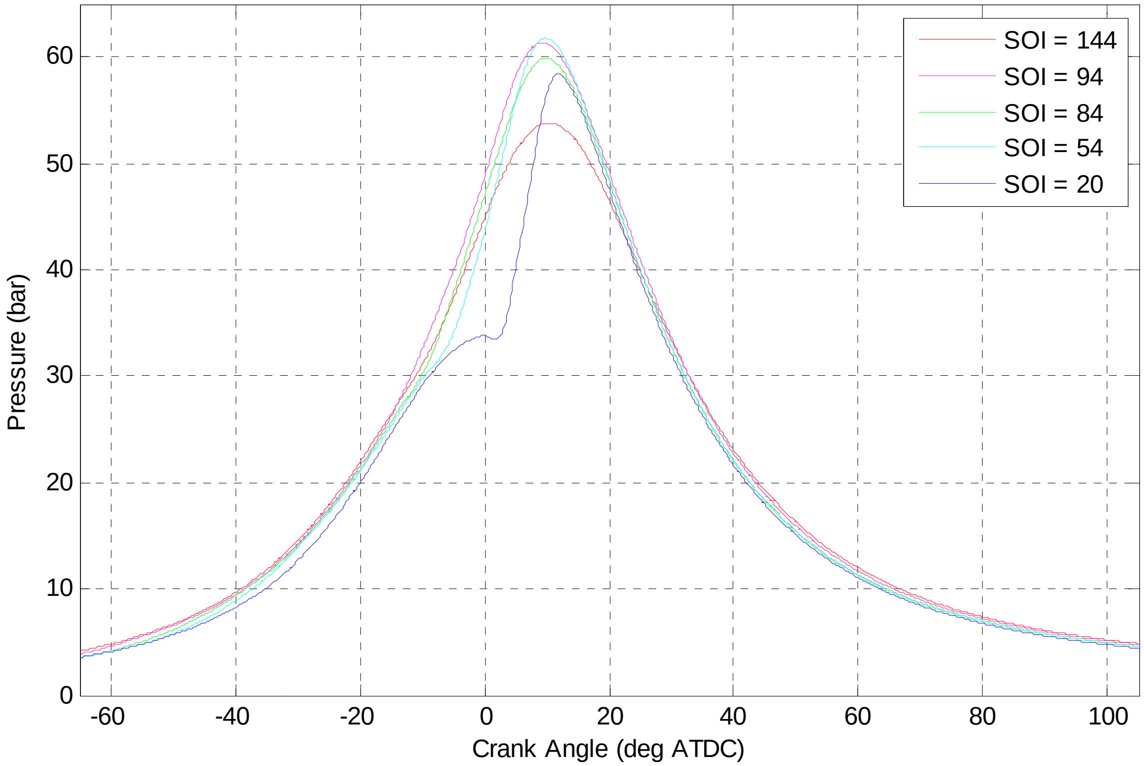

Figure 6.9: Pressure data as a function of crank angle for the EOI timings of Figure 6.8 (listed in degrees BTDC) for the dual-side-ignition/3+3H engine configuration.

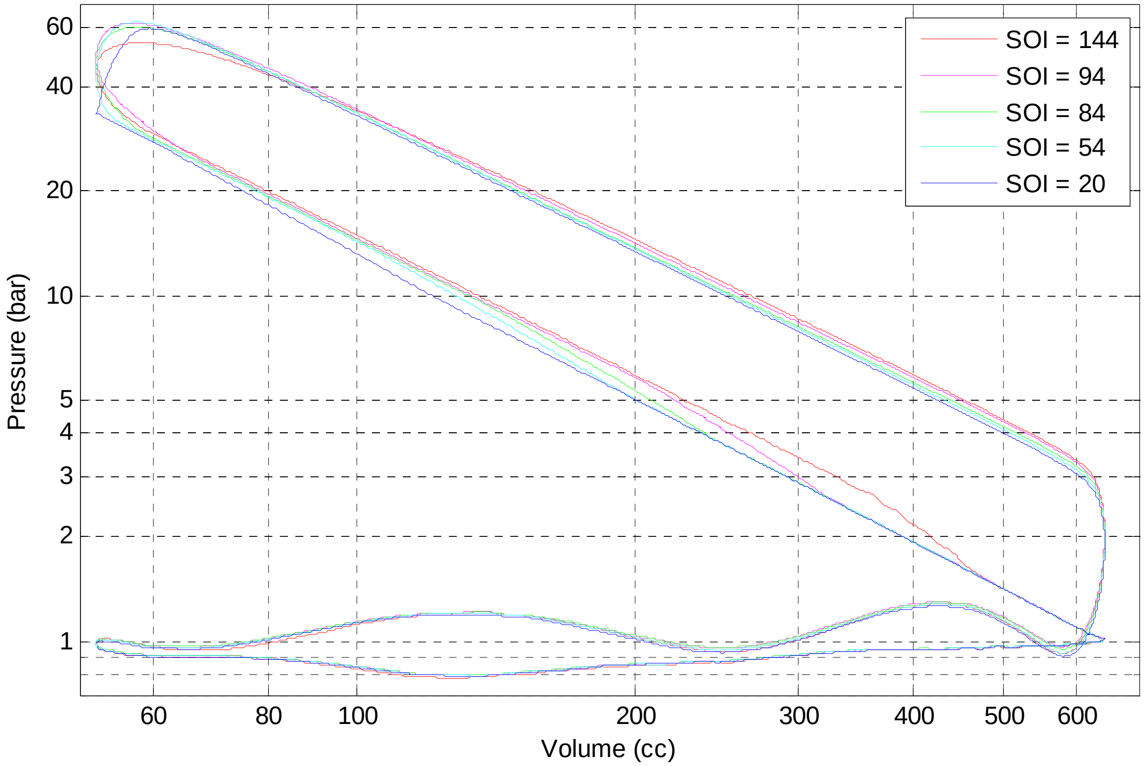

Figure 6.10: Pressure/volume time histories of selected EOI timings (listed in degrees BTDC) for the dual-side-ignition/3+3H engine configuration. The data correspond to the results presented in Figure 6.9.

Figures 6.9 and 6.10 highlight the tradeoff between:

- high pneumatic energy recovery, which occurs with late SOI
- fast combustion, which results from favorably stratified fuel distribution (generally late SOI)
- low heat transfer to the cylinder, which results from low combustion temperatures (generally early SOI) and lean mixtures near the cylinder wall (varies with injection timing).

Whereas Figure 6.10 shows all cases on the same axis, Figure 6.11 separates the five graphs and highlights the combustion portion of the pressure-volume diagrams for the five cases. As the fuel charge was injected later in the compression stroke, the burn rate becomes faster. With a SOI of 38 degrees, both burn rate and NO_x were quite high, indicating high temperatures in cylinder. However, overall efficiency was low and expansion pressure was low, indicating high combustion losses to the cylinder wall.

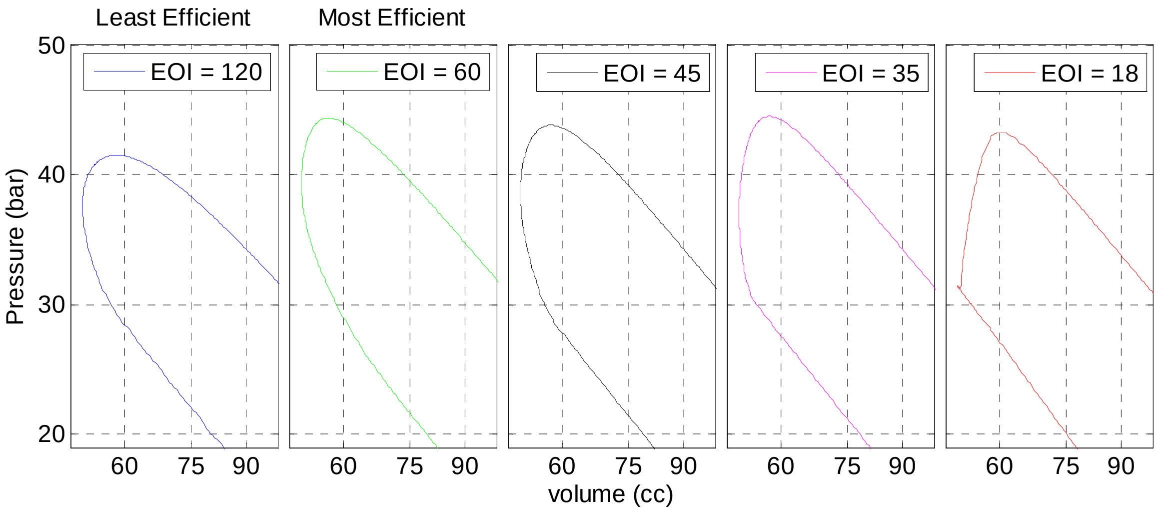

Figure 6.11: Pressure/volume time histories comparing earliest injection to latest injection for the dual-side-ignition/3+3H engine configuration.

Figures 6.12 and 6.13 compare the pV diagrams of the highest efficiency condition with the earliest injection condition (presumably the most homogeneous condition) and the latest injection timing tested (presumably quite stratified, as indicated by high levels of NO_x generation). When compared to the earliest-injection-condition, the best efficiency condition has advantages in pneumatic recovery and burn rate. The high efficiency condition has lower pressure during the later phases of the exhaust stroke, suggesting relatively greater heat transfer to the chamber walls. When compared to the latest-injection-condition, the best efficiency condition has slight disadvantages in burn rate, and larger disadvantage in pneumatic recovery. But the high efficiency condition has higher pressure during the exhaust stroke, suggesting higher heat losses occur with the latest injection timing conditions.

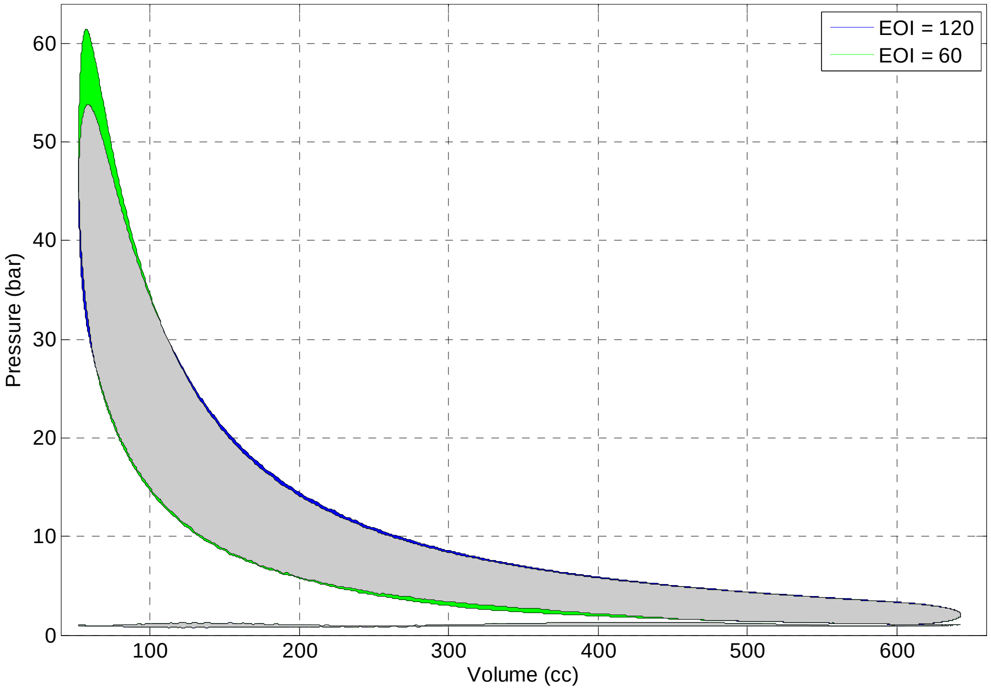

Figure 6.12: Comparison of pV diagrams for EOI = 120 degrees (near-homogeneous) and EOI = 60 degrees (best observed efficiency).

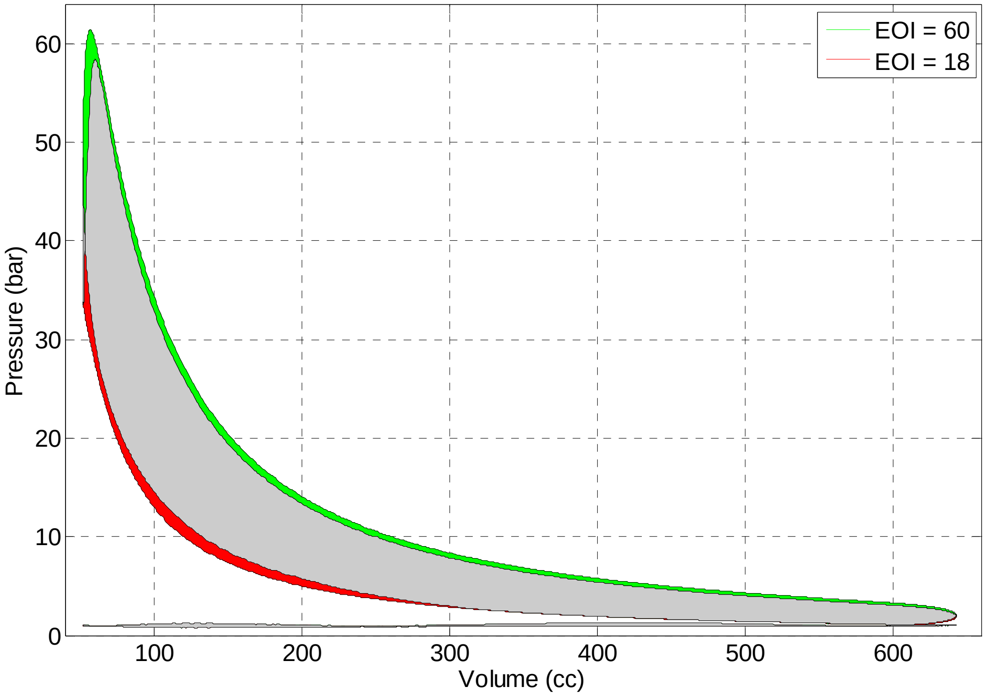

Figure 6.13: Comparison of pV diagrams for EOI = 60 degrees (best observed efficiency) and EOI = 18 degrees (highly stratified).

6.3.2 Effects of Engine Speed and Fuel Injector Orientation

Effects of engine speed and the orientation of the fuel injector were also investigated for the two cylinder head configurations and two fuel injector geometries. Only the results of the 3+3H injector and dual side ignition are presented here. The indicated thermal efficiency for the 3+3 injector and the dual side ignition at 3000 RPM, $\phi = 0.4$, and injector nozzle angle $\beta = 0$ (nozzles pointed towards ignition) is repeated in Figure 6.14 as a function of SOI. Also shown are the results for 3000 RPM, $\phi = 0.4$ and $\beta = 90$ (nozzles pointed perpendicular to the ignition axis), and the results for 1500 RPM, $\phi = 0.4$ and $\beta = 0$. The efficiency of the 3000 RPM and $\beta = 90$ condition shows the expected inverted-U shape. The efficiency of the 1500 RPM and $\beta = 0$ condition is not what is traditionally seen. There is a local maxima at approximately SOI = 90 degrees, a local minima when SOI = 63 degrees, the global maxima at SOI = 38 degrees, and the local minima when SOI = 28 degrees. Both the 1500 RPM/$\beta = 0$ and the 3000 RPM/$\beta = 0$ have two distinct maxima of efficiency; but the global maxima occur at earlier SOI for the 3000 RPM and at later SOI for the 1500 RPM case.

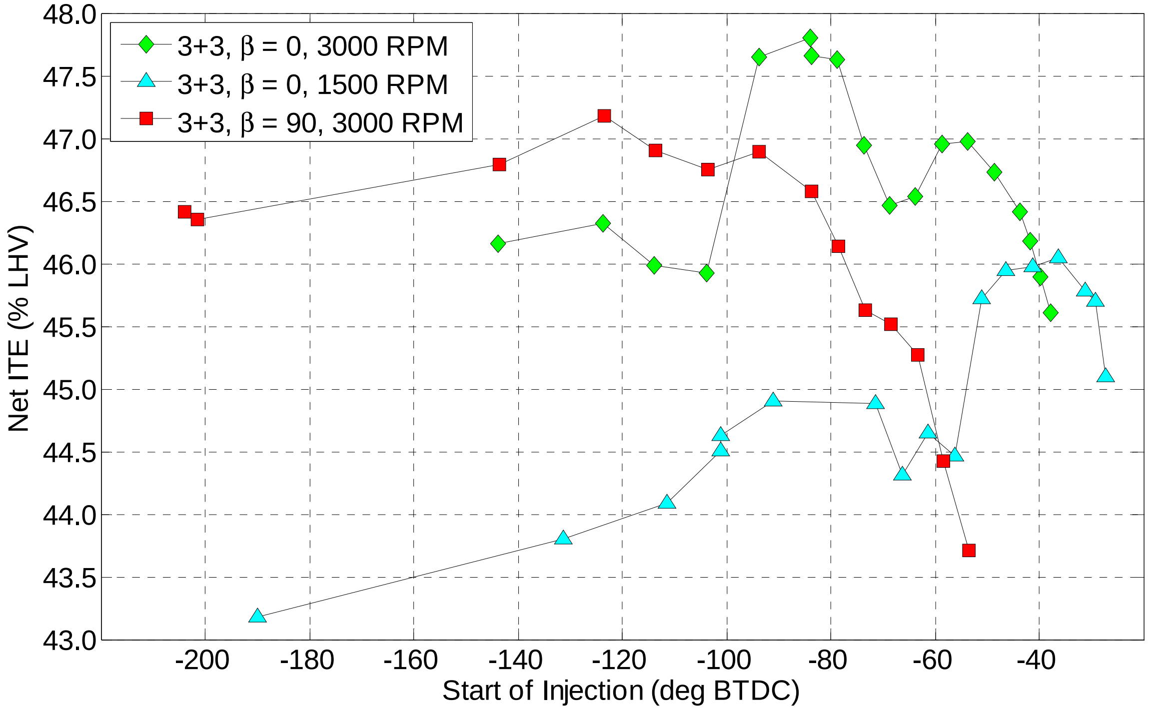

Figure 6.14: Thermal efficiency as a function of start of injection for different engine speeds and fuel injector orientations.

Figure 6.15 shows the correlation between 0-10% burn duration and SOI for the three cases presented in Figure 6.14. For 1500 RPM/β = 0, there is an unusual and distinct global maxima at approximately 60 degrees SOI. This slow kernel growth suggests that the fuel-air mixture is quite lean near the ignition sites. The 17 degrees for 10% burn contrasts starkly with the 12 degrees observed for the near-homogeneous mixture (190 degrees SOI) and the 5 degrees required for stratified injection timing (28 degrees SOI).

Figure 6.16 shows the 10-90% burn duration as a function of SOI. For 1500 RPM/β = 0, there is a small global maxima at approximately 70° SOI. The 3000//β = 90 condition shows an unusual trend towards slow burn at later injection timings.

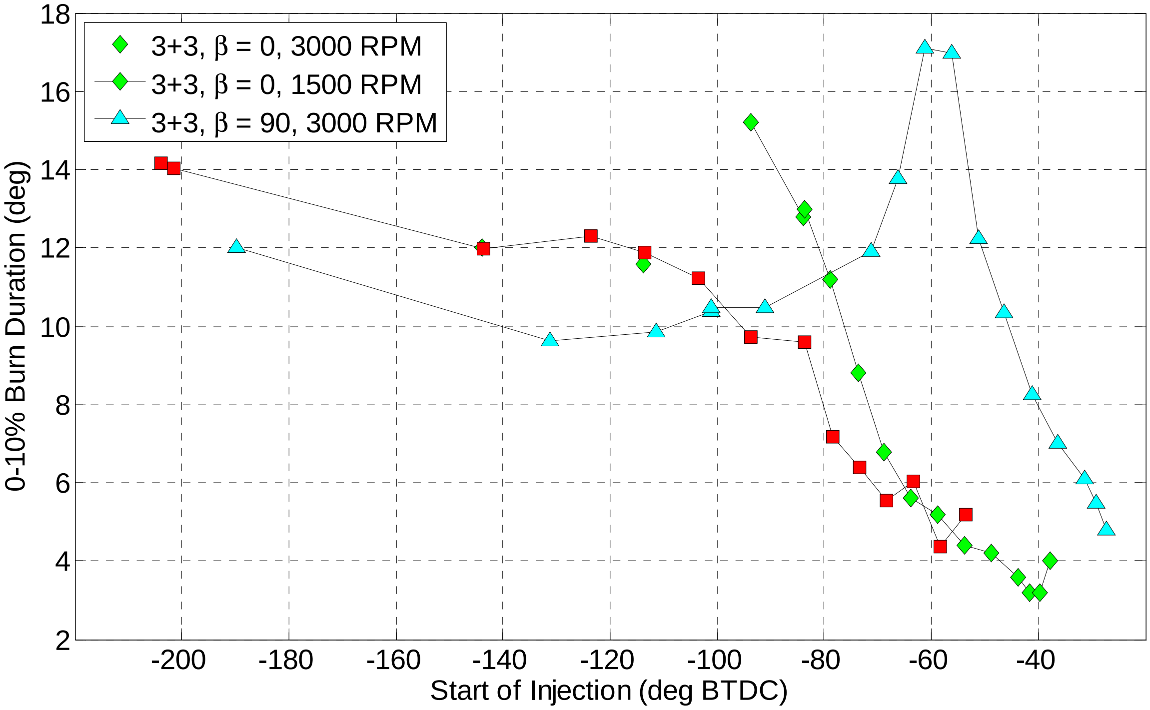

Figure 6.15: 0-10% burn duration as a function of SOI.

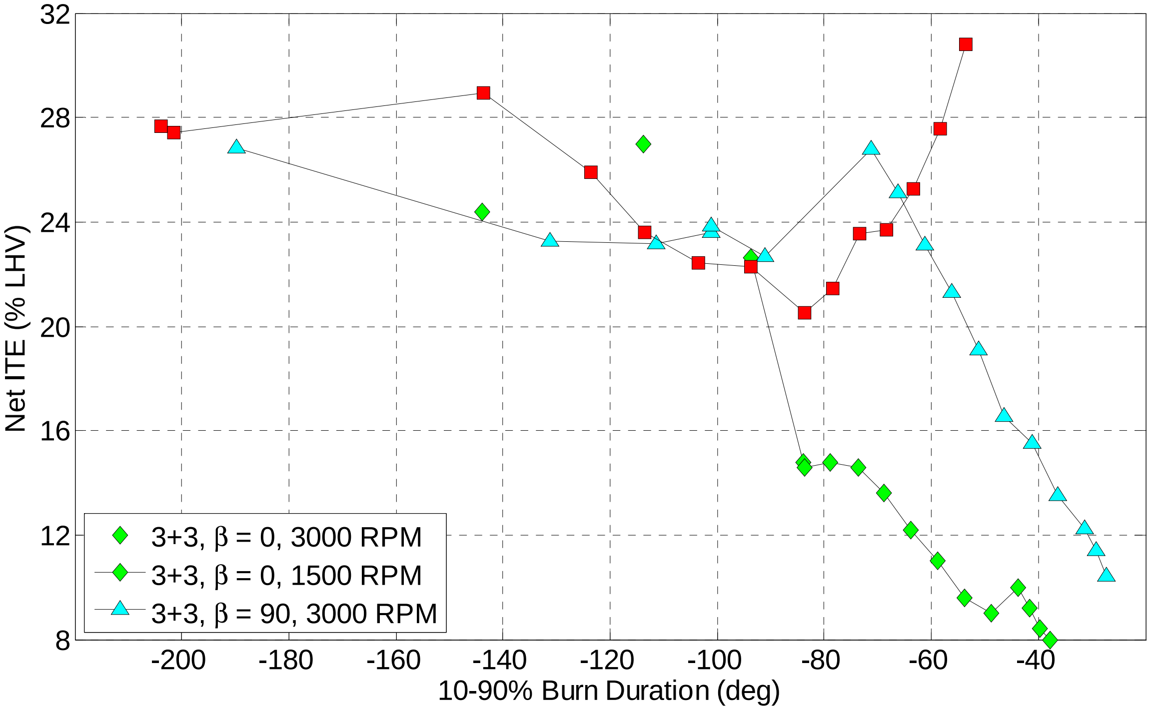

Figure 6.16: 10-90% burn duration as a function of SOI.

Figure 6.17 presents the combustion stability data for the different engine speed and fuel injector orientations. For the 1500 RPM/β = 0 conditions, there is a distinct maxima in instability at 66 degrees SOI. For 3000/β = 90, the latest injection timings show the highest instabilities. All other conditions showed good combustion stability.

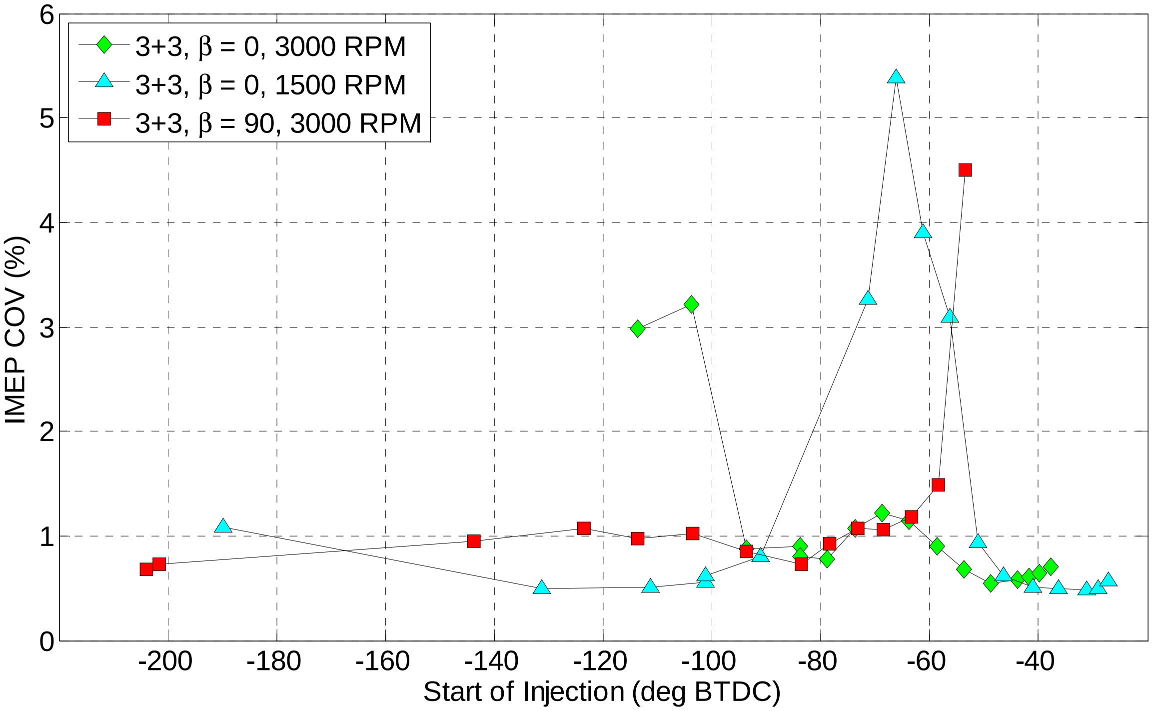

Figure 6.17: Combustion stability (COV of IMEP, % basis) as a function of SOI.

When considering the combustion statistics of Figure 6.17, some points are slightly vexing. At 1500 RPM/β = 0, some of the latest injection timings combine good combustion stability with superior burn rate, (for both 0-10% and 10-90% burn durations), yet have poor efficiency relative to similar conditions. The high NOx at this condition, coupled with the poor efficiency, suggests high temperature and proportionately large heat transfer to the cylinder walls.

Figure 6.18 shows the exhaust runner temperature as a function of SOI. None of the trends are strictly monotonic. At 1500 RPM/β = 0, there is a local maxima of heat rejection into the exhaust at 63 degrees SOI. At 3000 RPM/β = 90, there is a local maxima at 85 degrees SOI, and an uptick at 55 degrees SOI. For the other two conditions, last few points with the latest SOI conditions show level EGT as a function of SOI.

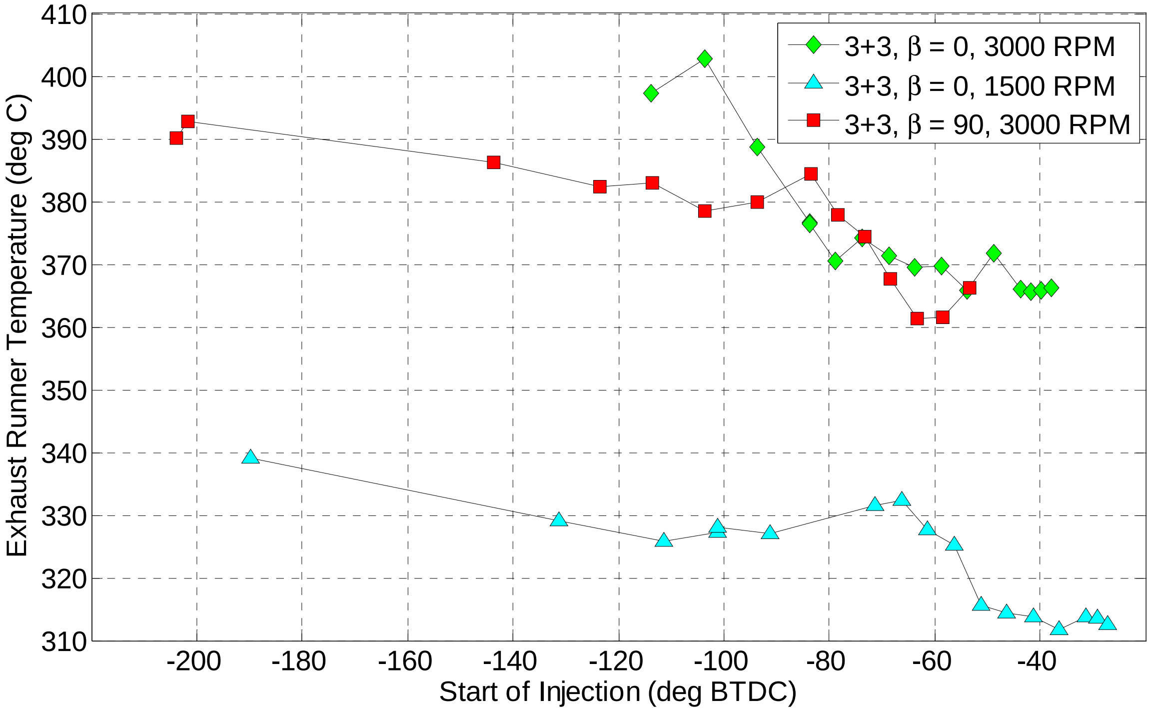

Figure 6.18: Exhaust runner temperature as a function of start of injection.

Figure 6.19 shows the increase in engine coolant temperature as a function of the SOI for the different engine speeds and fuel injector orientations. Although the flow rate of the pump was not directly recorded for these data, the pump settings remained constant for all tests and the results are expected to be qualitatively indicative of the heat rejected to the coolant. For all tests, the lowest speed/β = 0 conditions (the conditions expected to be the most homogeneous) show the least heat rejection into the coolant. For both β = 0 cases, there is an increase in the coolant temperature for the final few SOIs tested, indicating high heat transfer to the coolant. All three conditions show relatively constant heat rejection between 90 and 45 degrees SOI, and in the case of the 1500 RPM/ β = 0, relatively constant heat rejection between 90 and 30 degrees SOI.

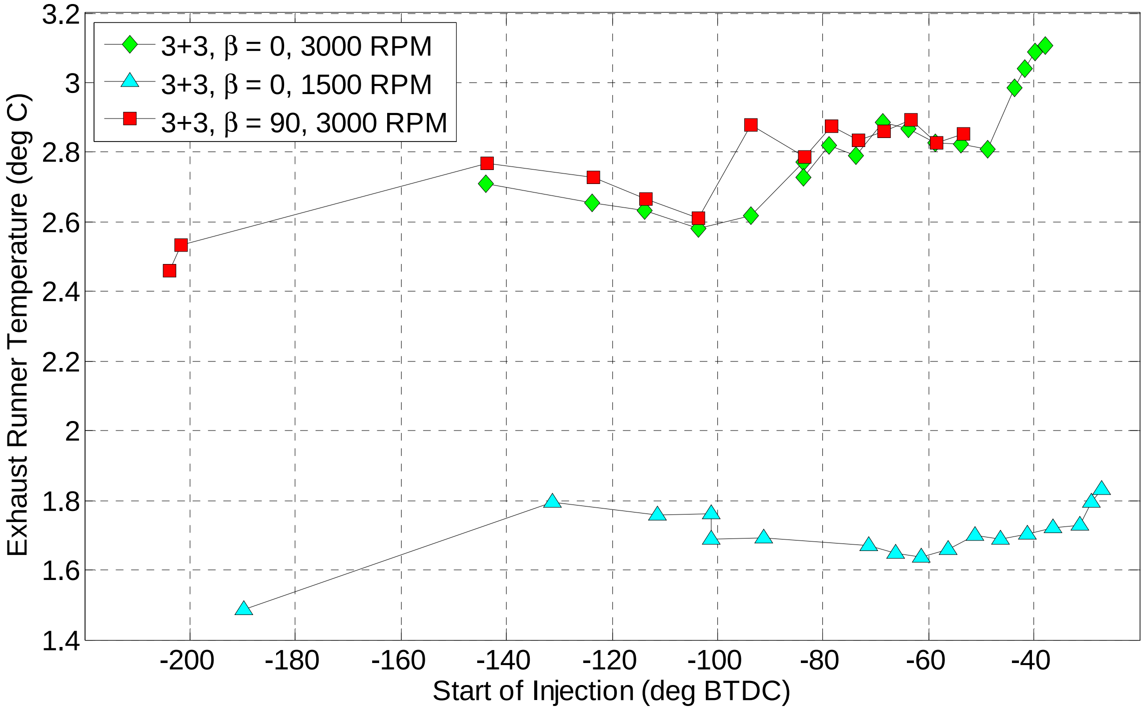

Figure 6.19: Increase in coolant temperature as a function of start of injection.

6.4 Summary and Conclusions

Different hardware configurations for cylinder head and fuel injector were experimentally characterized in these hydrogen engine studies. Engine performance was characterized by power, efficiency, and NOx exhaust gas emissions. Improvements in H_2 IC engine efficiency were demonstrated. The new combustion system using the dual plug cylinder head and the 3+3 fuel injector delivered a remarkable peak indicated thermal efficiency of 47.8%. At this condition, the NO_x emissions were 208 ppm. Other slightly sub-optimal conditions resulted in a 47.7% indicated thermal efficiency, while simultaneously reducing NO_x to 51 ppm. The mechanisms for the improvement are not completely understood, but the combustion characteristics, specifically the 10-

90% burn duration, show large improvements (with much shorter burn durations; on the order of a factor of 3) with the new combustion system. The results also indicate that, possibly as a result of the small boundary layers/low quenching distance of hydrogen, heat transfer plays a large role in differentiating engine efficiency as a function of fuel injector nozzle design, ignition location(s), and fuel injection timing. The combustion stability was good for all operating conditions, and the range of stable operation was improved with the new combustion system.

The engine performance was a strong function of the SOI for each hardware configuration. Earlier SOI presumably yields more time for mixing and hence more homogeneous H_2/air mixtures. Reducing the mixing time by using later SOI timing, leads to more stratified mixtures. The burn rates, NO_x emissions, and exhaust runner temperatures all suggest the bulk of the fuel is combusted in stratified (relatively) rich zones. Optical engine studies, presented in the following chapter, provide further insight into the mixing processes important in determining the magnitude and mechanisms of the hydrogen fuel distribution.

Chapter 7

Optical Characterization of Fuel Distribution in the Dual Zone Combustion System

7.1 Introduction

The performance of the dual zone combustion system has been shown to vary considerably with phasing of fuel injection. Some conditions, namely 3000 RPM and 85 degree SOI, combine short burn durations, high efficiency and low NOx emissions. When the fuel is injected much later, less than 30 degrees BTDC, burn durations remain short, but efficiency is poor. Moreover, the decline between best and worst efficiency is not monotonic, but rather is characterized by local maxima and minima. This interesting behavior warranted optical characterization of the hydrogen fuel distribution.

7.2 Optical Engine Experimental Setup

All optical experiments were conducted at the Sandia National Laboratories in Livermore, California. This work was the result of a collaboration between Ford Motor Company, Sandia National Lab, and Westport Innovations. All optical experiments were conducted in collaboration with Victor Salazar.

The engine, dynamometer, and associated equipment used has been the test bed for many hydrogen fueled experiments over the past seven years [8], [19], [20], [23–25], [35–38].

7.2.1 Engine Hardware

The engine specifications are shown in Table 7.1 and are contrasted with the specifications of the metal H2 IC engine at Ford Motor Company used for the studies presented in Chapters 3-6.

Location	Ford		Sandia	
Engine Type	Metal		Optical	
Max Engine Speed	6000		1500	RPM
Combustion Chamber	Pentroof		Pentroof	
Valvetrain	DOHC 4V		DOHC 4V	
Compression Ratio	10.4-15.7		11	
Bore	89		92	mm
Stroke	78	95	85	mm
Displacement	486	592	565	cc

Table 7.1: Comparison of Metal Engine and Optical Engine.

For all the optical experiments conducted at Sandia, the fuel distribution was characterized without ignition. The engine, complete with quartz liner and quartz piston, are shown in Figure 7.2 together with a schematic. Since the optical studies that will be shown in this chapter are all recorded without ignition, the cylinder head could be considered an approximation of either the single or dual ignition cylinder head presented previously. All tests shown in this chapter were completed with the same 3+3 injector used for experiments in chapter 6, shown again in Figure 7.2.

Detailed specifications of the experimental setup and analytical process are given in [20] and are briefly summarized here.

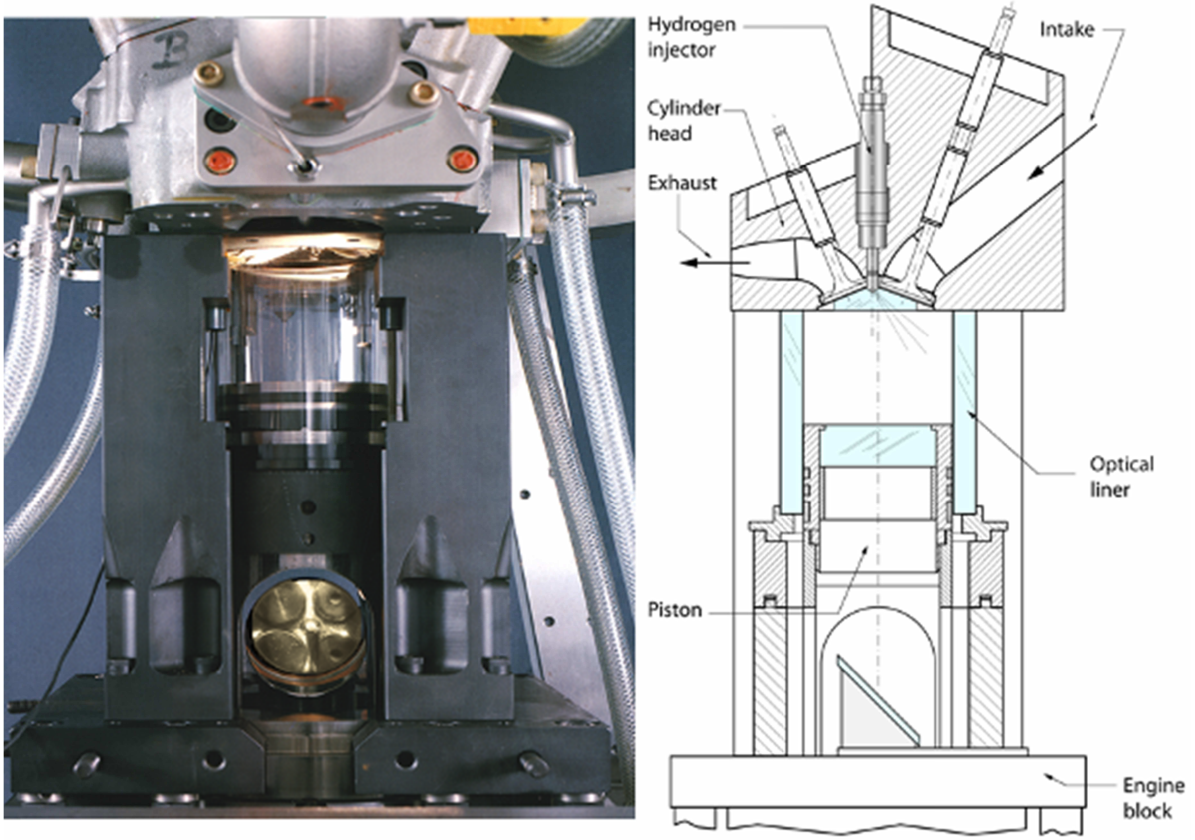

Figure 7.1: Test Engine at Sandia National Lab and Schematic, Courtesy Victor Salazar.

	
Pattern	3+3
Spray Angle	45/70
Nozzle Diameter (mm)	0.545
Nozzle Area (mm^2)	0.233
Total Flow Area (mm^2)	1.4

Figure 7.2: Injector used in experiments.

7.2.2 Fuel Distribution Characterization

In order to characterize the fuel distribution, the fuel was seeded with acetone at high pressure. The justification of using acetone as a tracer is detailed in [20] and is summarized with a table showing pertinent characteristics in Table 7.2. Although the diffusion coefficient of hydrogen (0.73 cm^2/s) is much larger than that of any of the three fuel tracers considered, an order of magnitude error analysis showed that the diffusion coefficient was unlikely to be critical in large-scale fuel distribution images averaged over several cycles [20].

	Acetone	Toluene	TEA
Mol. Mass [g/mol]	58.1	92.1	101.1
Boiling point at 1 bar [K]	329.4	383.8	361.9
Saturation concentration in H_2 at 100 bar, 300K [% Vol.]	0.33	0.042	0.10
Diffusion Coefficient [cm^2/s]	0.11	0.079	0.072
Excitation wavelengths [nm]	230 - 320	240 - 270	Max. at 240
Emission wavelengths [nm]	325 - 500	270 - 320	270 - 330

Table 7.2: Comparison of Possible Fuel Tracers [20]**.**

The optical path of the laser used for imaging is shown in Figure 7.3. This testing setup was well established at Sandia prior to the work described here.[20] A Nd:YAG laser produced pulses of approximately 200 mJ of energy at 8 ns of duration at a frequency of 10 Hz. The laser itself was frequency quadrupled from 1060 nm to 266 nm. A mechanical shutter ensured that pulses not synchronized with the engine speed did not reach the experiment. A Pellin-Brocca prism filtered out the remaining 532 nm light, reducing the lasers energy to approximately 160 mJ. After passing through the prism, the laser entered a passive-cavity beam stretcher via a translucent mirror with an R/T of 37/63. The passive cavity beam stretcher distributed the energy of excitation in order to maximize energy while avoiding component (i.e. cylinder liner) damage. In the passive cavity beam stretcher, two lenses, with focal lengths of 1000mm and -750mm, were employed to re-collimate the laser beam. In total, the passive cavity stretcher reduced the peak instantaneous energy of the laser by a factor of 2.5.[20] A half-wave attenuator allowed further fine-tuning of laser energy to the desired total output of approximately 125 mJ. A cylindrical (planar) lens with a focal length of -300mm transformed the laser from a column of light to a sheet of light. A lens of focal length 1500 mm served two purposes. First, the lens focused the sheet of light on the experiment, reducing the thickness of the sheet of light to approximately 600 µm. Second, a intentionally introduced small deviation from perpendicularity enabled a small amount of light to be reflected towards a Coherent LabMax TOP (J25-MUV-193 sensor) energy meter. The energy meter recorded the relative energy of each laser pulse, which was later used in post-processing to normalize each image's recorded fluorescence to the total laser energy transmitted to the experiment. Two apertures were employed, both after the 1500mm lens and before the energy meter, in order to minimize aberrant light. A periscope was used to align the laser with the plane of measurement desired.

Images were recorded with a Princeton Instruments PIXIS 1024B, which used an unintensified back-illuminated CCD to record fluorescent intensity. For horizontal images, a 85mm lens with an aperture of f/1.4 was used with an auxiliary close-focusing lens, as is shown in Figure 7.3. For vertical images, a 55mm f/1.2 lens was substituted and of course the camera orientation and cylindrical lens orientation were changed.

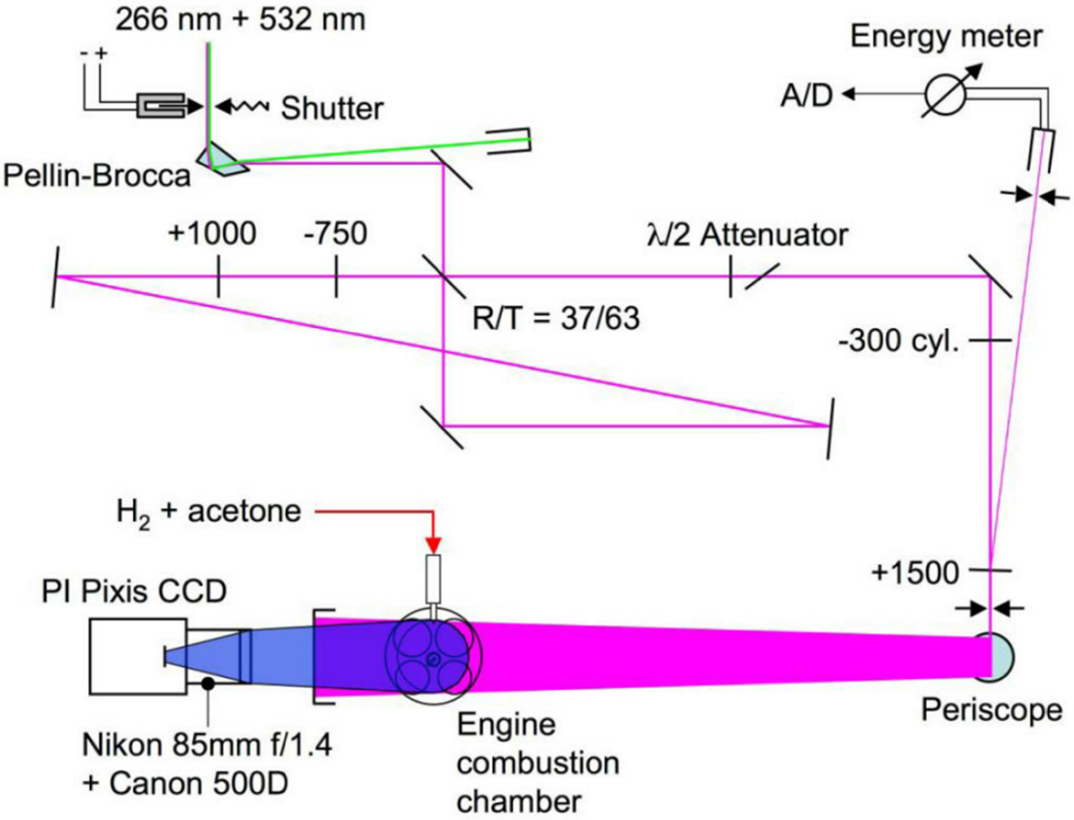

Figure 7.3: Schematic of Laser Setup for Imaging [20]**.**

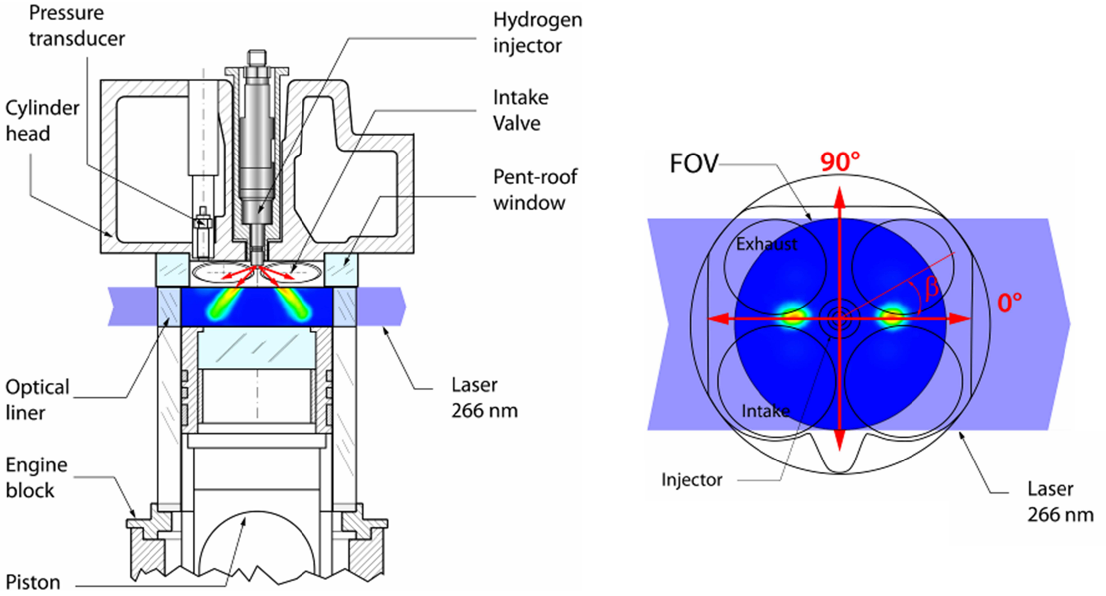

Figure 7.4: Test Setup Schematics and example vertical (left) and horizontal (right) images. Figure courtesy Victor Salazar.

Figure 7.4 shows two example images superimposed into their respective positions within the combustion chamber. As can be seen, the field of view (FOV) for both images does not extend to the edges of the combustion chamber. The image taken through the cylinder liner ('vertical') does not extend into the combustion chamber, and the picture taken through the piston ('horizontal') only shows 65mm of the 92mm bore, or 50% of the projected area of the cylinder.

The definition used to characterize the fuel injector orientation is also presented in Figures 7.4 and 7.5. The angle of orientation of the fuel injector, β, corresponds to 0 degrees when the holes of the fuel injector are aligned with the axis of the two spark plugs. When the holes of the fuel injector are orthogonal to the axis of ignition, β is defined as 90 degrees. Figure 7.5 also highlights the ignition locations, which are outside the field of view of the camera.

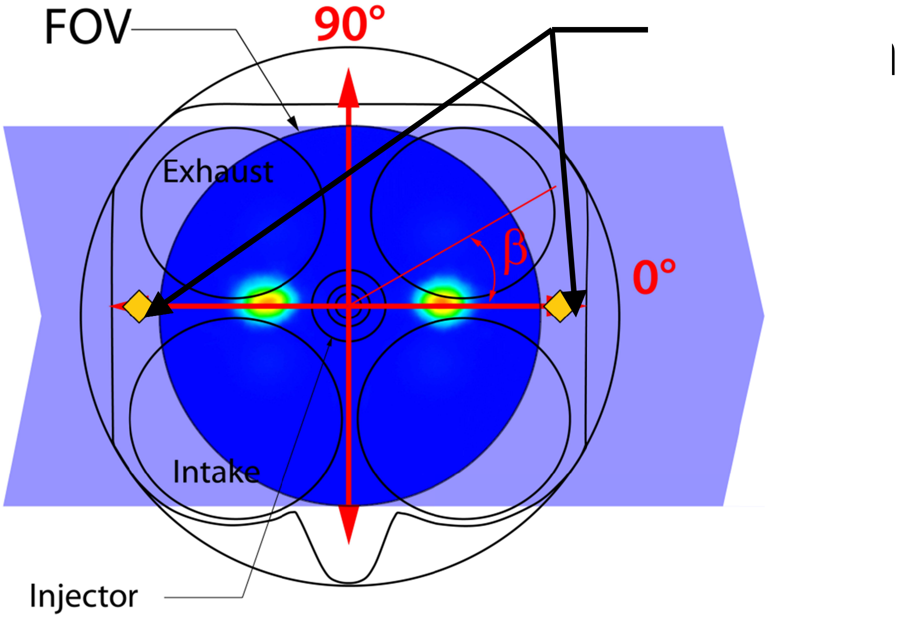

Figure 7.5: Location of spark plugs in Dual-Side Ignition Cylinder Head.

Figure 7.6 details the vertical image and the six planes at which horizontal images were taken. Note that the vertical image has been stretched along the cylinder axis in order to completely show the horizontal images.

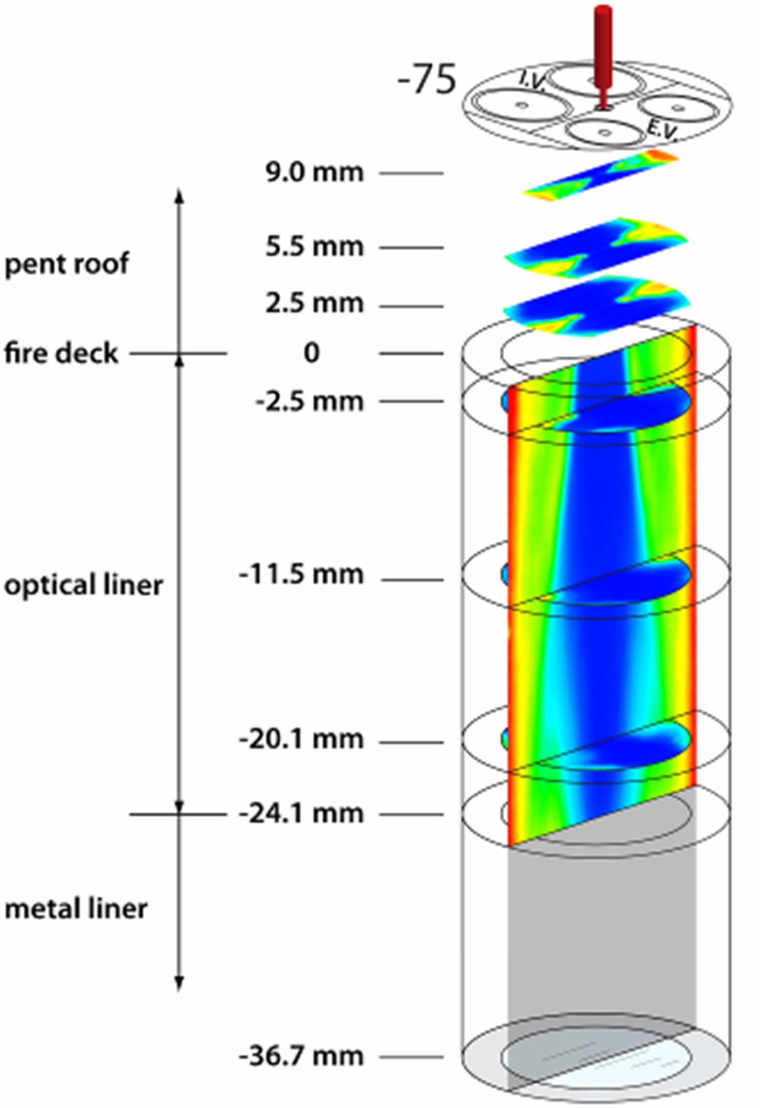

Figure 7.6: Relative Positions of Vertical and Horizontal images.

7.2.3 Imaging Procedure

In order to appropriately interpret the data, every dataset began with an image of a near-homogenous fuel distribution where the global equivalence ratio was $\phi = 1.5$. This image was followed by an image taken without injecting fuel. The two images were used to 'span' and 'zero' the imaging data, respectively.

Two images were then acquired of the fuel distribution to be characterized. The referencing process was then repeated to acquire a second set of 'span' and 'zero', followed by two more characterization images. This process was repeated 50 times for a total of 200 images, and is shown graphically in Figure 7.7. Between each of the 200 images, 4 engine cycles were run without imaging, in order to allow the laser and camera to appropriately sync with the engine speed. All tests were conducted without ignition of the fuel mixture.

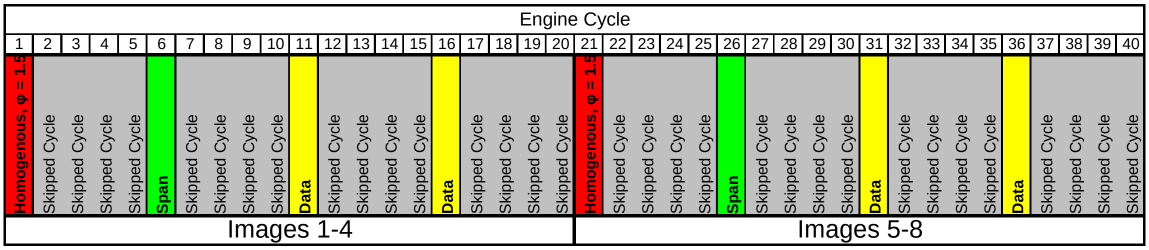

Figure 7.7: Timeline for 2 sets of four images taken. Process was repeated until a total of 200 images were taken.

7.3 Test Matrix

The optical engine was limited to a maximum engine speed of 1500 RPM. The metal engine results for indicated thermal efficiency for 1500 RPM as a function of start of injection timing at an equivalence ratio of ϕ= 0.4 are shown in Figure 7.8 and contrasted with the results at 3000 RPM. The approximate local minima and maxima for the 1500 RPM β= 0 condition were found at 90 degrees…, 63°, 38°, and 28° BTDC. These inflection points were chosen for the optical engine study. For β= 90°, SOI timings of 90 degrees…, 63°, and 38° were selected. Due to concerns of combustion stability, 28° SOI was not investigated for β= 90. Metal-engine tests were not conducted with β= 90° at 1500 RPM at Ford Motor Company. Nevertheless, data at 3000 RPM and data taken in conjunction with Argonne National Labs suggest that operation at SOI=90° has good efficiency and is characterized by NOx levels similar to that of homogeneous operation. Similar data and inferences suggest that β= 90° and

SOI=38° is unlikely to have good efficiency. At β= 90° and SOI =63°, the efficiency of the engine is very sensitive to minor changes in injection timing. Additionally, minor differences in bore and stroke can substantially affect fuel distribution at MBT, and thus no general claims as to the efficiencies of fuel distributions at these conditions are made.

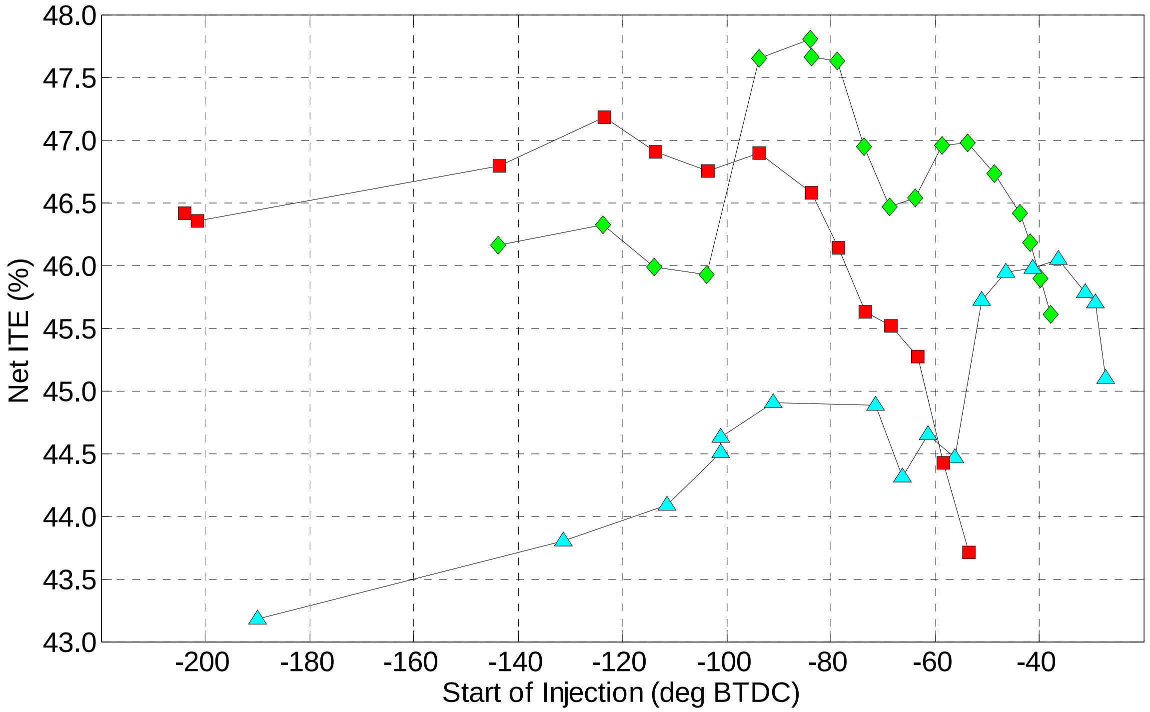

Figure 7.8: Efficiency as a function of Injection Phasing.

The test matrix of vertical and horizontal images taken is shown in Table 7.3. Both vertical and horizontal images were taken at regular intervals and at the ignition timing. In order to be able to characterize fuel penetration immediately after injection, finer steps were used after injection in the vertical plane. In total, images were taken for 255 different combinations of injector nozzle orientation, injection timing, imaging timing, and image plane.

		β = 0							β = 90						
Configuration		Vertical	Horizontal						Vertical	Horizontal					
Image Plane		Vertical	a	ab	b	c	d	e	Vertical	a	ab	b	c	d	e
SOI	Image CA														
28	25	🟩	🟩	🟩	🟩	🟩	▨	▨	⬜	⬜	⬜	⬜	⬜	⬜	⬜
	24	🟩	⬜	⬜	⬜	⬜	▨	▨	⬜	⬜	⬜	⬜	⬜	⬜	⬜
	23	🟩	⬜	⬜	⬜	⬜	▨	▨	⬜	⬜	⬜	⬜	⬜	⬜	⬜
	22	🟩	⬜	⬜	⬜	⬜	▨	▨	⬜	⬜	⬜	⬜	⬜	⬜	⬜
	21	🟩	⬜	⬜	⬜	⬜	▨	▨	⬜	⬜	⬜	⬜	⬜	⬜	⬜
	20	🟩	🟩	🟩	🟩	🟩	▨	▨	⬜	⬜	⬜	⬜	⬜	⬜	⬜
	15	🟩	🟩	🟩	🟩	▨	▨	▨	⬜	⬜	⬜	⬜	⬜	⬜	⬜
	11	▨	🟩	🟩	🟩	▨	▨	▨	⬜	⬜	⬜	⬜	⬜	⬜	⬜
	4	▨	🟩	🟩	🟩	▨	▨	▨	⬜	⬜	⬜	⬜	⬜	⬜	⬜
	1	▨	🟩	🟩	🟩	▨	▨	▨	⬜	⬜	⬜	⬜	⬜	⬜	⬜
38	35	🟩	🟩	🟩	🟩	🟩	▨	▨	🟩	🟩	🟩	🟩	🟩	▨	▨
	34	🟩	⬜	⬜	⬜	⬜	▨	▨	🟩	⬜	⬜	⬜	⬜	▨	▨
	33	🟩	⬜	⬜	⬜	⬜	▨	▨	🟩	⬜	⬜	⬜	⬜	▨	▨
	32	🟩	⬜	⬜	⬜	⬜	▨	▨	🟩	⬜	⬜	⬜	⬜	▨	▨
	31	🟩	⬜	⬜	⬜	⬜	▨	▨	🟩	⬜	⬜	⬜	⬜	▨	▨
	30	🟩	🟩	🟩	🟩	🟩	▨	▨	🟩	🟩	🟩	🟩	🟩	▨	▨
	25	🟩	🟩	🟩	🟩	🟩	▨	▨	🟩	🟩	🟩	🟩	🟩	▨	▨
	20	🟩	🟩	🟩	🟩	🟩	▨	▨	🟩	🟩	🟩	🟩	🟩	▨	▨
	15	🟩	🟩	🟩	🟩	▨	▨	▨	🟩	🟩	🟩	🟩	▨	▨	▨
	11	▨	🟩	🟩	🟩	▨	▨	▨	▨	🟩	🟩	🟩	▨	▨	▨
	4	▨	🟩	🟩	🟩	▨	▨	▨	▨	🟩	🟩	🟩	▨	▨	▨
	-1	▨	🟩	🟩	🟩	▨	▨	▨	▨	⬜	⬜	⬜	▨	▨	▨
63	61	🟩	⬜	⬜	⬜	⬜	⬜	⬜	🟩	⬜	⬜	⬜	⬜	⬜	⬜
	60	🟩	🟩	🟩	🟩	🟩	🟩	🟩	🟩	🟩	🟩	🟩	🟩	🟩	🟩
	59	🟩	⬜	⬜	⬜	⬜	⬜	⬜	🟩	⬜	⬜	⬜	⬜	⬜	⬜
	58	🟩	⬜	⬜	⬜	⬜	⬜	⬜	🟩	⬜	⬜	⬜	⬜	⬜	⬜
	57	🟩	⬜	⬜	⬜	⬜	⬜	⬜	🟩	⬜	⬜	⬜	⬜	⬜	⬜
	56	🟩	⬜	⬜	⬜	⬜	⬜	⬜	🟩	⬜	⬜	⬜	⬜	⬜	⬜
	55	🟩	⬜	⬜	⬜	⬜	⬜	⬜	⬜	⬜	⬜	⬜	⬜	⬜	⬜
	48	⬜	⬜	⬜	⬜	⬜	⬜	▨	🟩	⬜	⬜	⬜	⬜	⬜	▨
	45	🟩	🟩	🟩	🟩	🟩	🟩	▨	🟩	🟩	🟩	🟩	🟩	🟩	▨
	40	⬜	⬜	⬜	⬜	⬜	▨	▨	🟩	⬜	⬜	⬜	⬜	▨	▨
	35	🟩	⬜	⬜	⬜	⬜	▨	▨	⬜	⬜	⬜	⬜	⬜	▨	▨
	30	🟩	🟩	🟩	🟩	🟩	▨	▨	🟩	🟩	🟩	🟩	🟩	▨	▨
	25	🟩	🟩	🟩	🟩	🟩	▨	▨	⬜	⬜	⬜	⬜	⬜	▨	▨
	20	🟩	🟩	🟩	🟩	🟩	▨	▨	🟩	🟩	🟩	🟩	🟩	▨	▨
	15	🟩	🟩	🟩	🟩	▨	▨	▨	🟩	⬜	⬜	⬜	▨	▨	▨
	11	▨	🟩	🟩	🟩	▨	▨	▨	▨	🟩	🟩	🟩	▨	▨	▨
90	88	🟩	⬜	⬜	⬜	⬜	⬜	⬜	🟩	⬜	⬜	⬜	⬜	⬜	⬜
	87	🟩	⬜	⬜	⬜	⬜	⬜	⬜	⬜	⬜	⬜	⬜	⬜	⬜	⬜
	86	🟩	⬜	⬜	⬜	⬜	⬜	⬜	⬜	⬜	⬜	⬜	⬜	⬜	⬜
	85	🟩	⬜	⬜	⬜	⬜	⬜	⬜	🟩	⬜	⬜	⬜	⬜	⬜	⬜
	84	🟩	⬜	⬜	⬜	⬜	⬜	⬜	⬜	⬜	⬜	⬜	⬜	⬜	⬜
	83	🟩	⬜	⬜	⬜	⬜	⬜	⬜	⬜	⬜	⬜	⬜	⬜	⬜	⬜
	82	🟩	⬜	⬜	⬜	⬜	⬜	⬜	⬜	⬜	⬜	⬜	⬜	⬜	⬜
	80	🟩	⬜	⬜	⬜	⬜	⬜	⬜	🟩	⬜	⬜	⬜	⬜	⬜	⬜
	78	🟩	⬜	⬜	⬜	⬜	⬜	⬜	⬜	⬜	⬜	⬜	⬜	⬜	⬜
	76	🟩	⬜	⬜	⬜	⬜	⬜	⬜	⬜	⬜	⬜	⬜	⬜	⬜	⬜
	75	🟩	🟩	🟩	🟩	🟩	🟩	🟩	🟩	🟩	🟩	🟩	🟩	🟩	🟩
	72	⬜	⬜	⬜	⬜	⬜	⬜	⬜	🟩	⬜	⬜	⬜	⬜	⬜	⬜
	68	🟩	⬜	⬜	⬜	⬜	⬜	⬜	🟩	⬜	⬜	⬜	⬜	⬜	⬜
	65	⬜	⬜	⬜	⬜	⬜	⬜	⬜	🟩	⬜	⬜	⬜	⬜	⬜	⬜
	60	🟩	🟩	🟩	🟩	🟩	🟩	🟩	🟩	🟩	🟩	🟩	🟩	🟩	🟩
	55	🟩	⬜	⬜	⬜	⬜	⬜	⬜	🟩	⬜	⬜	⬜	⬜	⬜	⬜
	40	⬜	⬜	⬜	⬜	⬜	⬜	▨	🟩	⬜	⬜	⬜	⬜	⬜	▨
	45	🟩	🟩	🟩	🟩	🟩	🟩	▨	🟩	🟩	🟩	🟩	🟩	🟩	▨
	30	🟩	🟩	🟩	🟩	🟩	▨	▨	🟩	🟩	🟩	🟩	🟩	▨	▨
	25	🟩	⬜	⬜	⬜	⬜	▨	▨	🟩	⬜	⬜	⬜	⬜	▨	▨
	20	🟩	🟩	🟩	🟩	🟩	▨	▨	🟩	🟩	🟩	🟩	🟩	▨	▨
	15	🟩	⬜	⬜	⬜	▨	▨	▨	🟩	⬜	⬜	⬜	▨	▨	▨
	11	▨	🟩	🟩	🟩	▨	▨	▨	▨	🟩	🟩	🟩	▨	▨	▨

Legend
🟩 Data
⬜ No Data
▨ Impracticable

Table 7.3: Matrix of Tests Conducted for optical imaging studies.

7.4 Experimental Results

7.4.1 Injection Direction (β) = 0°

As was previously noted, efficiency is at a local maxima with β = 0° and SOI = 90° BTDC. The fuel distribution, characterized in horizontal planes, is shown in Figure 7.10 for a range of injection timings. Note that the values corresponding to maximum mole fractions in the images gradually decrease from 0.4 to 0.25. (The scale used in each case is noted at the bottom of the cylinder in each image stack. For reference, the conversion between equivalence ratio and molar fraction is shown in Figure 7.9.) The shift in scale improves the resolution of the relative fuel stratification over the widely changing local conditions. At the ignition timing of 11° BTDC, the images indicate a relatively homogeneous distribution, with some more lean locations towards the edges of the horizontal images.

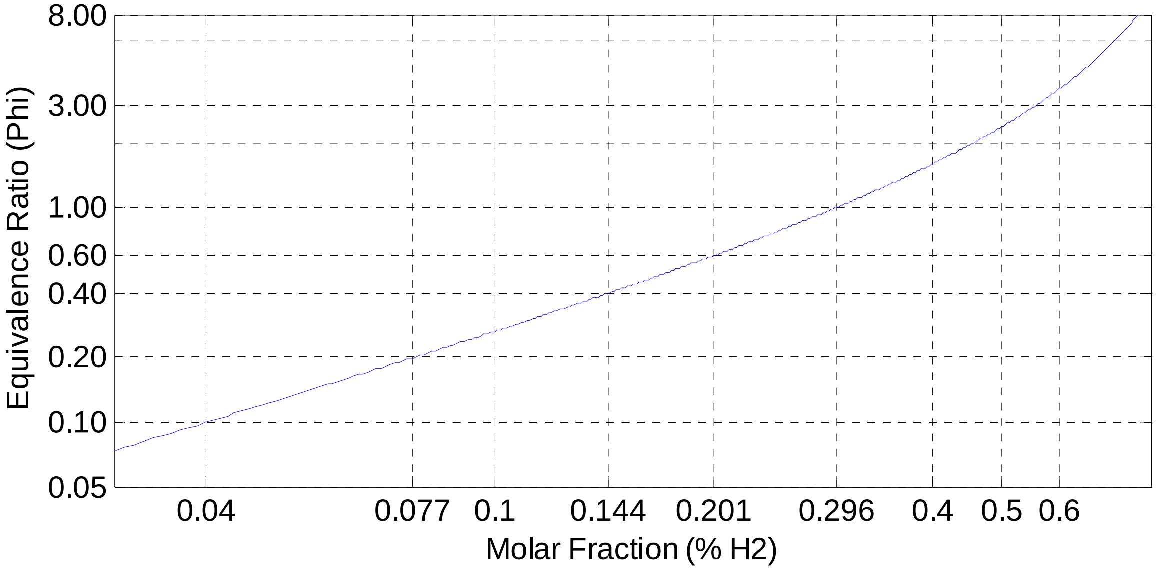

Figure 7.9: Equivalence Ratio as a function of Molar Fraction.

The vertical images that correspond to these conditions are superimposed upon the horizontal images in Figure 7.11. Under these conditions, the fuel impinges upon the cylinder wall. After impinging on the wall, and in some cases the piston, the fuel travels circumferentially along the cylinder wall and then re-impinges upon the fuel from the other group of 3 nozzles. At an angle of 45° BTDC the fuel is concentrated in the center of the combustion chamber, but that concentration is reduced somewhat before ignition timing is reached.

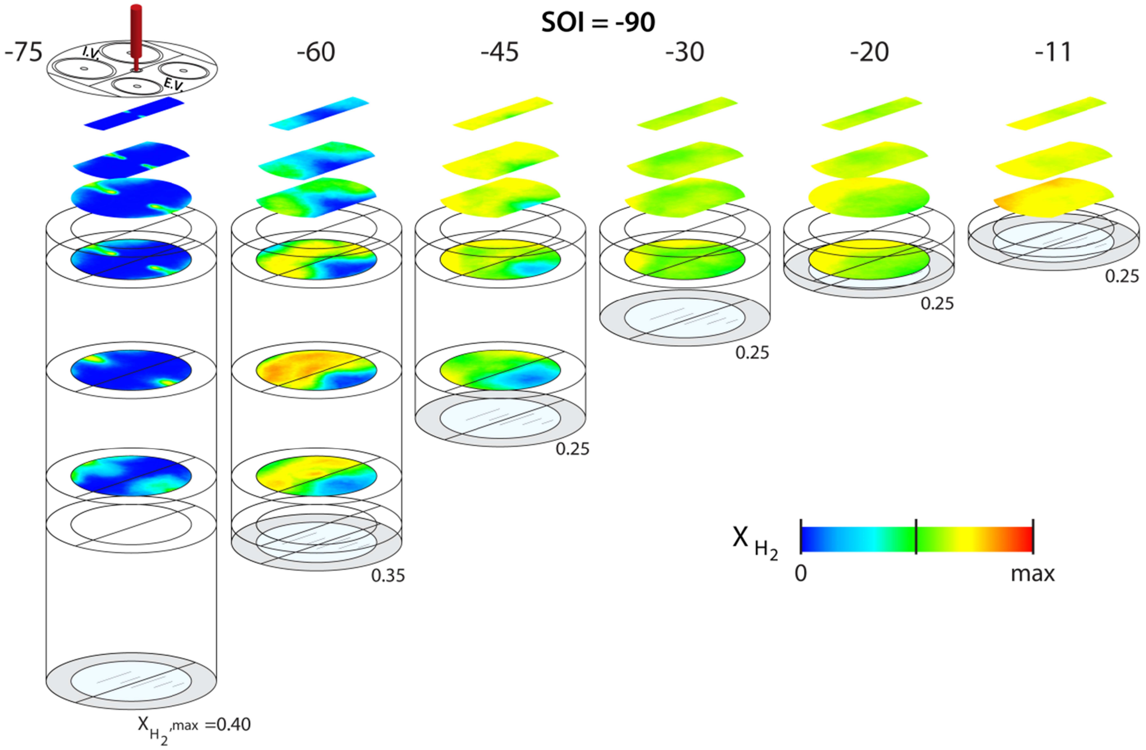

Figure 7.10: Fuel Distribution for SOI = 90° and β = 0°, Vertical planes only. Images taken at 75, 60, 45, 30, 20, and 11° BTDC. MBT Timing was found to be 11° BTDC for equivalent metal engine experiment. On the metal engine, this condition was found to be a local maxima of efficiency.

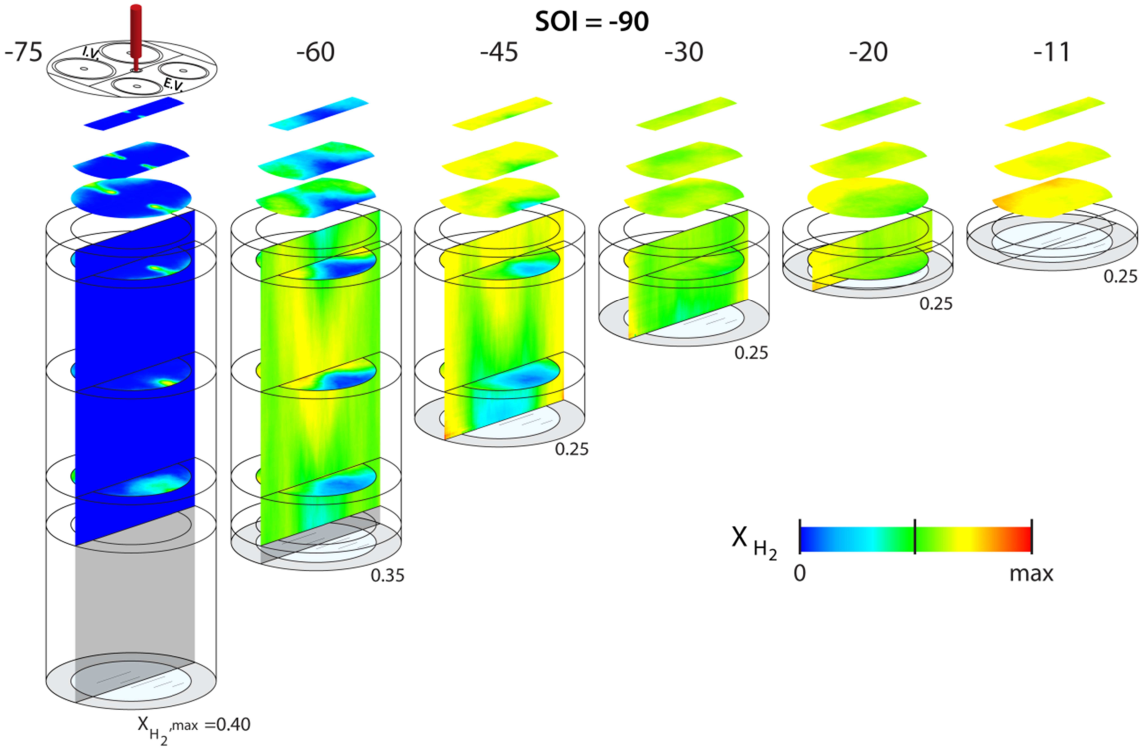

Figure 7.11: Fuel Distribution for SOI = 90° and β = 0°, vertical and horizontal planes. Images taken at 75, 60, 45, 30, 20, and 11° BTDC. MBT Timing was found to be 11° BTDC for equivalent metal engine experiment. On the metal engine, this condition was found to be a local maxima of efficiency.

The local minimum of efficiency was shown previously for the metal engine configuration to be approximately 63° BTDC. The fuel distribution at this condition is presented in Figures 7.12 and 7.13. For this injection timing, the metal engine testing resulted in an MBT of 11° BTDC. For the SOI = 63° BTDC conditions, the fuel travel begins in a manner similar to that at a SOI of 90°; where the fuel impinges upon the wall, re-impinges upon fuel from the other group of nozzles, and then concentrates in the center of the chamber. Unlike the SOI 90° conditions, this concentration in the center of the chamber is still strong at ignition timing. Although these conditions would be good for a centrally located spark plug, the fuel distribution was not conducive to dual-side-ignition.

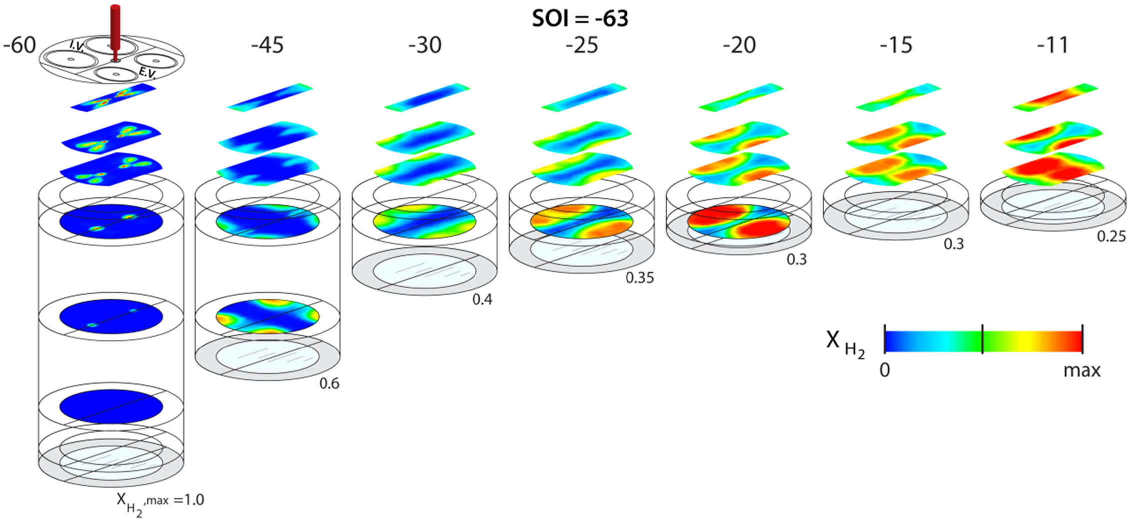

Figure 7.12: Fuel Distribution for SOI = 63° and β = 0°, horizontal planes only. Images taken at 60, 45, 30, 25, 20, 15, and 11° BTDC. MBT Timing was found to be 11° BTDC for equivalent metal engine experiment. On the metal engine, this condition was a local minima of efficiency.

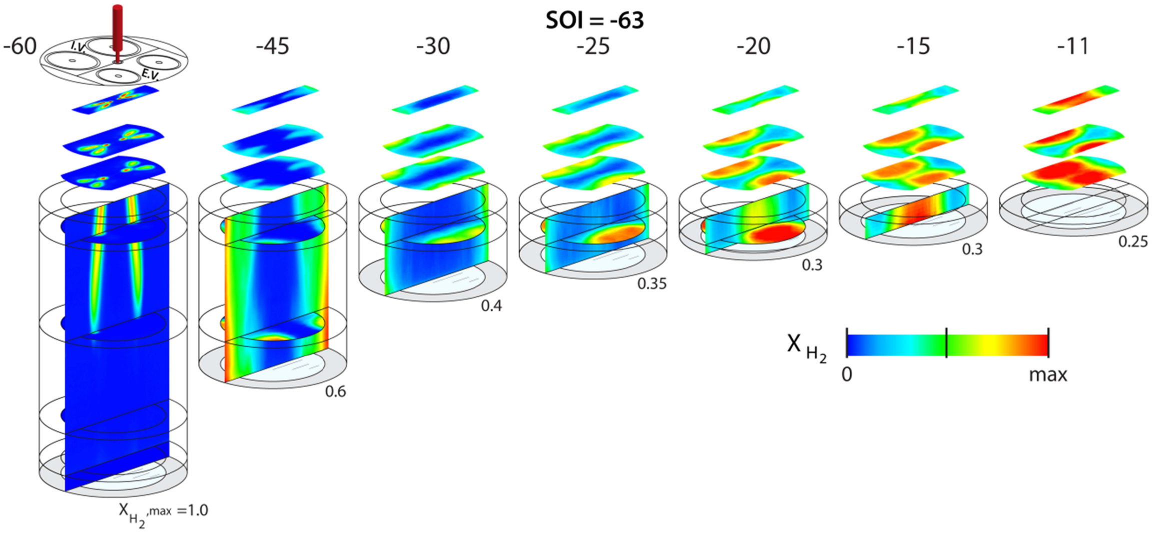

Figure 7.13: Fuel Distribution for SOI = 63° BTDC and β = 0°, horizontal and vertical planes. Images taken at 60, 45, 30, 25, 20, 15, and 11° BTDC. MBT Timing was found to be 11° BTDC for equivalent metal engine experiment. On the metal engine, this condition condition was found to be a local minima of efficiency.

Figures 7.14 and 7.15 show the fuel distribution at 38° BTDC with β = 0°. On the metal engine, this condition showed the highest efficiency of all points tested at 1500 RPM. The fuel impinges on the piston and the cylinder wall. Unlike the previous two conditions, only a portion of the fuel travels circumferentially around the cylinder wall. The majority of the fuel remains near the edges of the cylinder at which the injector nozzles were directed. The mole fraction near the ignition locations was approximately 0.22.

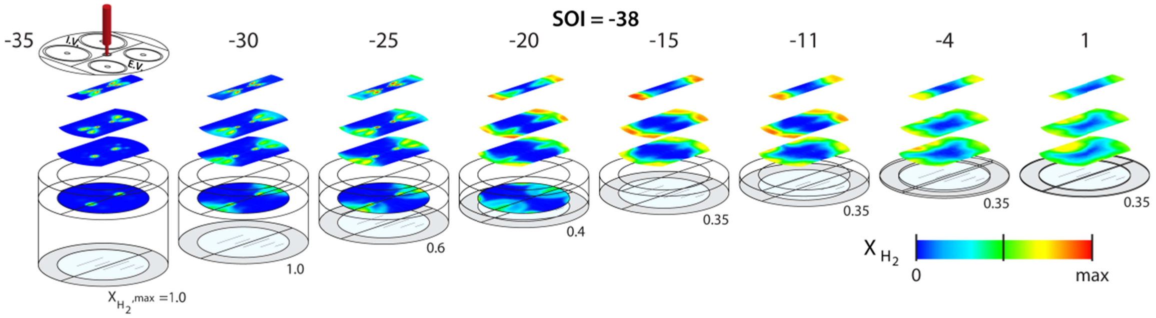

Figure 7.14: Fuel Distribution for SOI = 38° BTDC and β = 0°, horizontal planes only. Images taken at 35, 30, 25, 20, 15, 11, 4° BTDC and 1° ATDC. MBT Timing was found to be 1° ATDC for equivalent metal engine experiment. On the metal engine, this condition was found to have the highest efficiency of all points tested.

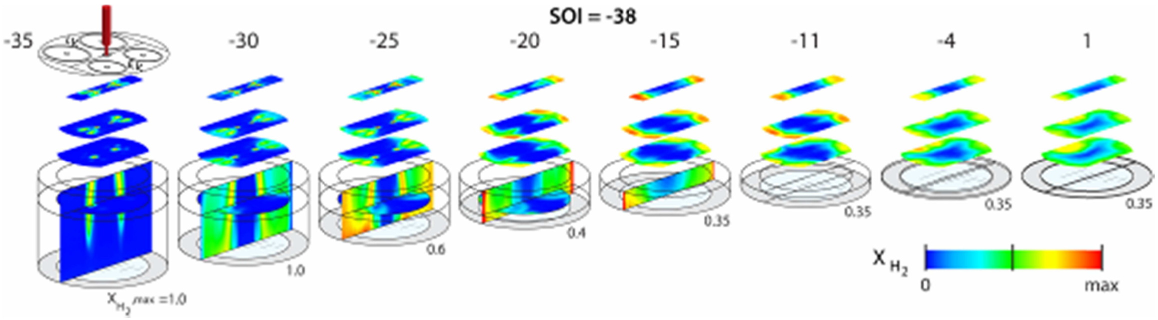

Figure 7.15: Fuel Distribution for SOI = 38° BTDC and β = 0°, horizontal and vertical planes. Images taken at 35, 30, 25, 20, 15, 11, 4° BTDC and 1° ATDC. MBT Timing was found to be 1° ATDC for equivalent metal engine experiment. On the metal engine, this condition was found to have the highest efficiency of all points tested.

Figures 7.16 and 7.17 show the fuel distribution resulting from a SOI of 28° BTDC. At this injection timing, the vast majority of the fuel remains near the spark plugs at which the nozzles were directed. The mole fraction of fuel near the ignition sites was over 0.3; indicating a mixture slightly richer than stoichiometric. The temperatures encountered by burning a mixture at this equivalence ratio would be quite high and likely result in a large amount of heat being transferred to the cylinder walls.

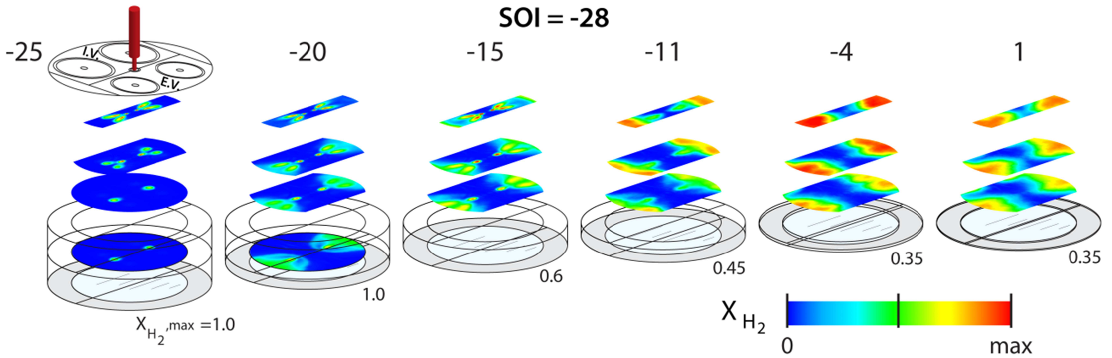

Figure 7.16: Fuel Distribution for SOI = 28° BTDC and β = 0°, horizontal planes only. Images taken at 25, 20, 15, 11, 4° BTDC and 1° ATDC. MBT Timing was found to be 1° ATDC for equivalent metal engine experiment. On the metal engine, this condition was found to have poor efficiency.

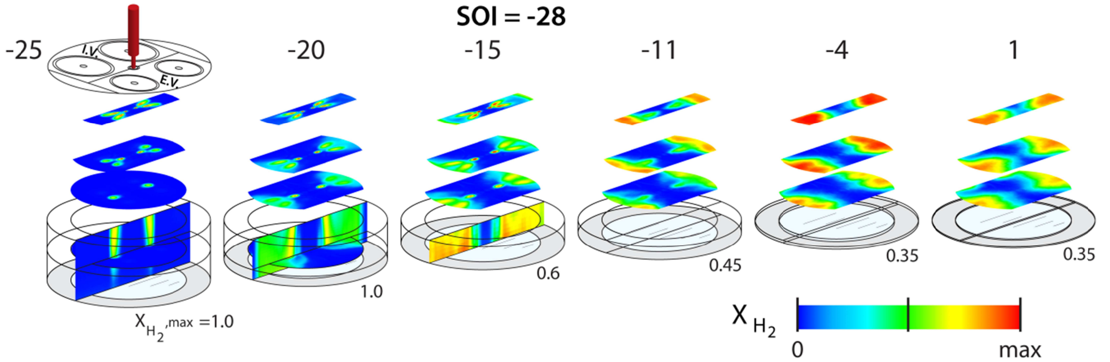

Figure 7.17: Fuel Distribution for SOI = 28° BTDC and β = 0°, horizontal and vertical planes. Images taken at 25, 20, 15, 11, 4° BTDC and 1° ATDC. MBT Timing was found to be 1° ATDC for equivalent metal engine experiment. On the metal engine, this condition was found to have poor efficiency.

7.4.2 Injection Direction (β) = 90°

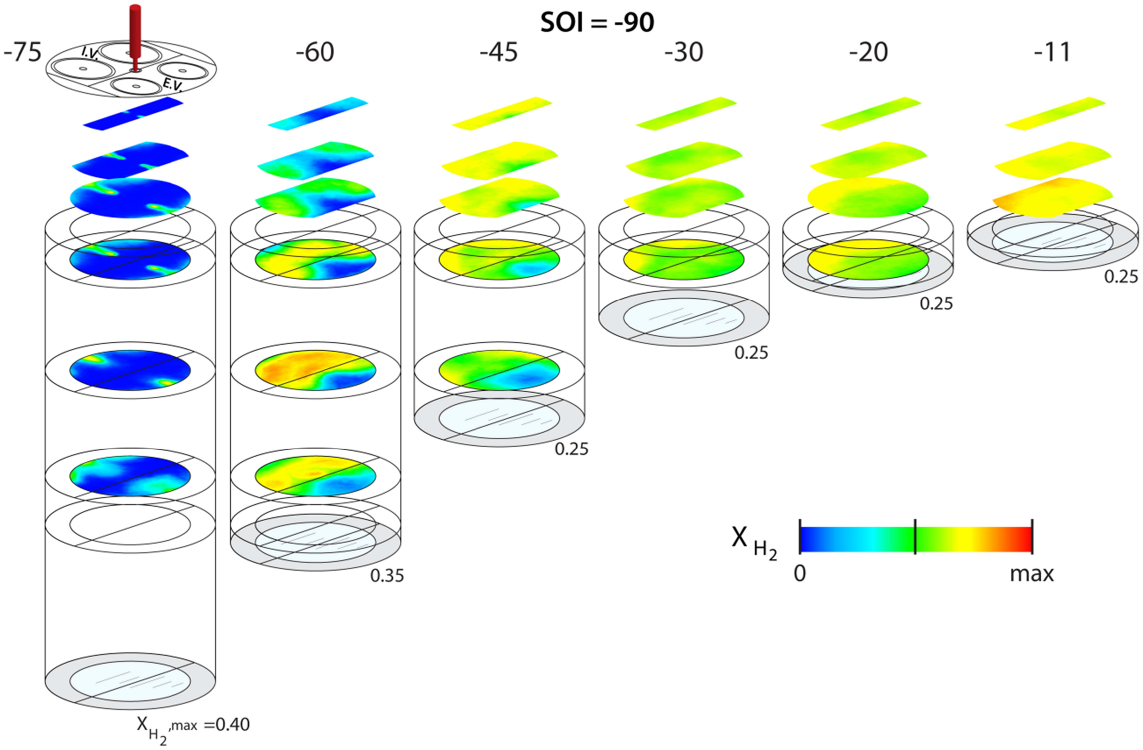

Figure 7.18: Fuel Distribution for SOI = 90° BTDC and β = 90°, horizontal planes only. Images taken at 75, 60, 45, 30, 20 and 11°BTDC. Metal engine testing completed outside the scope of this work indicated this point would be less efficient than SOI = 63°.

Figures 7.18-7.23 show the fuel distribution with the injection nozzle orientation (β) rotated along the injector axis by 90°. Figures 7.18 and 7.19 present the fuel distribution when the injection timing is 90° BTDC. After impinging on the cylinder wall (and in some cases the piston), the fuel again travels circumferentially around the piston, with the most stratified locations being slightly biased towards the intake valves. This bias is thought to be due to the non-symmetric pentroof chamber rather than bulk motion of the gas; the low tumble ratio of the engine combined with the high momentum of the fuel makes bulk-gas-motion-effects unlikely. In any case, at the ignition timing of 11° BTDC the fuel distribution is close to homogeneous.

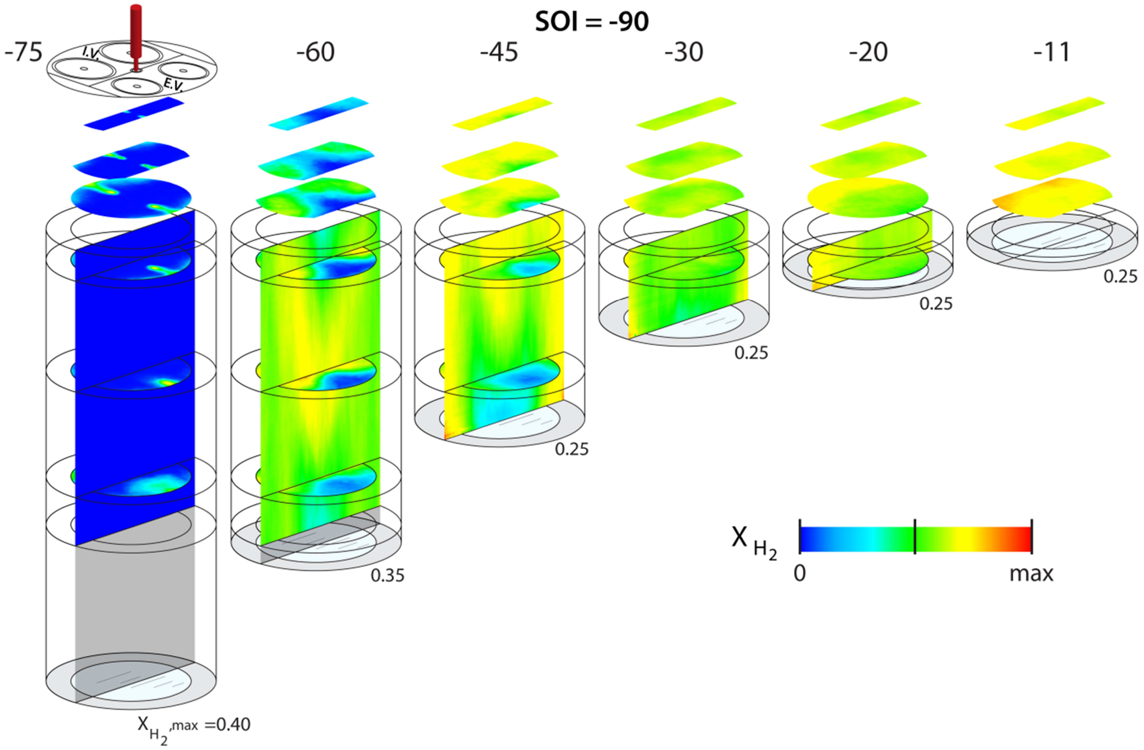

Figure 7.19: Fuel Distribution for SOI = 90° BTDC and β = 90°, horizontal planes only. Images taken at 75, 60, 45, 30, 20 and 11°BTDC. Metal engine testing done outside the scope of this work indicated this point would be less efficient than SOI = 63°.

Figures 7.20 and 7.21 show the results at a SOI of 63° BTDC. The fuel impinges on the cylinder wall and piston. It travels circumferentially along the wall until impinging with the fuel from the other set of nozzles, at which point fuel travel slows. At the ignition timing of 11° BTDC, there are rich zones, with a mole fraction of approximately 0.25, near each of the spark plugs.

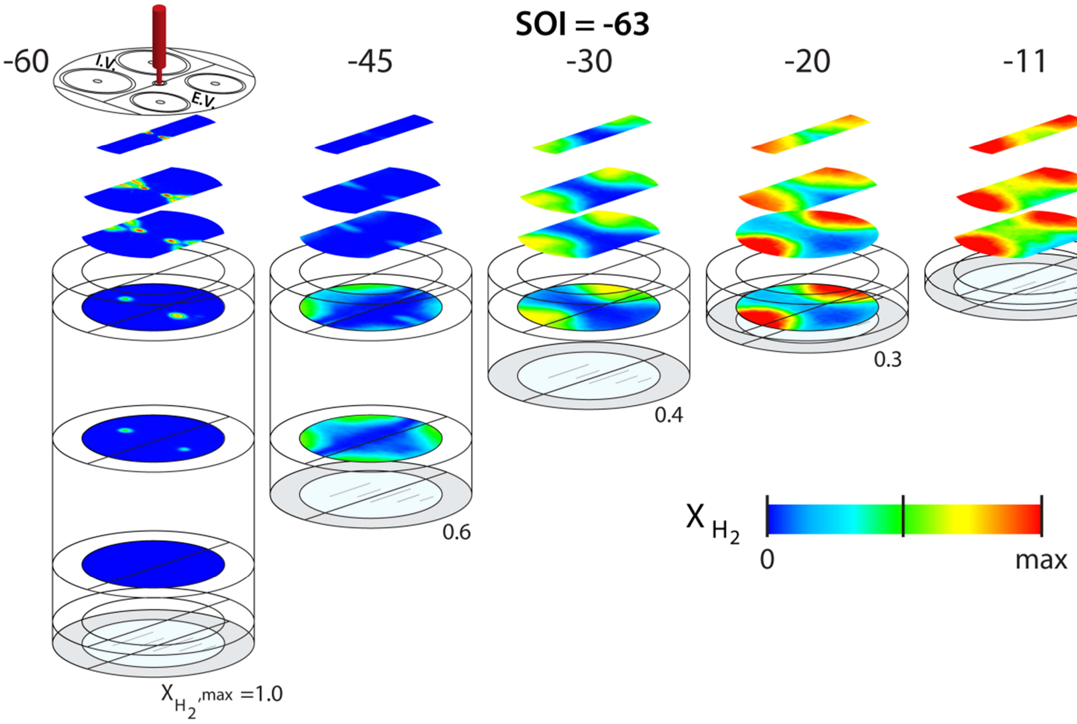

Figure 7.20: Fuel Distribution for SOI = 63° BTDC and β = 90°, horizontal planes only. Images taken at 60, 45, 30, 20 and 11° BTDC. Metal engine testing done outside the scope of this work indicated this condition is close to the peak efficiency point of SOI = 70°.

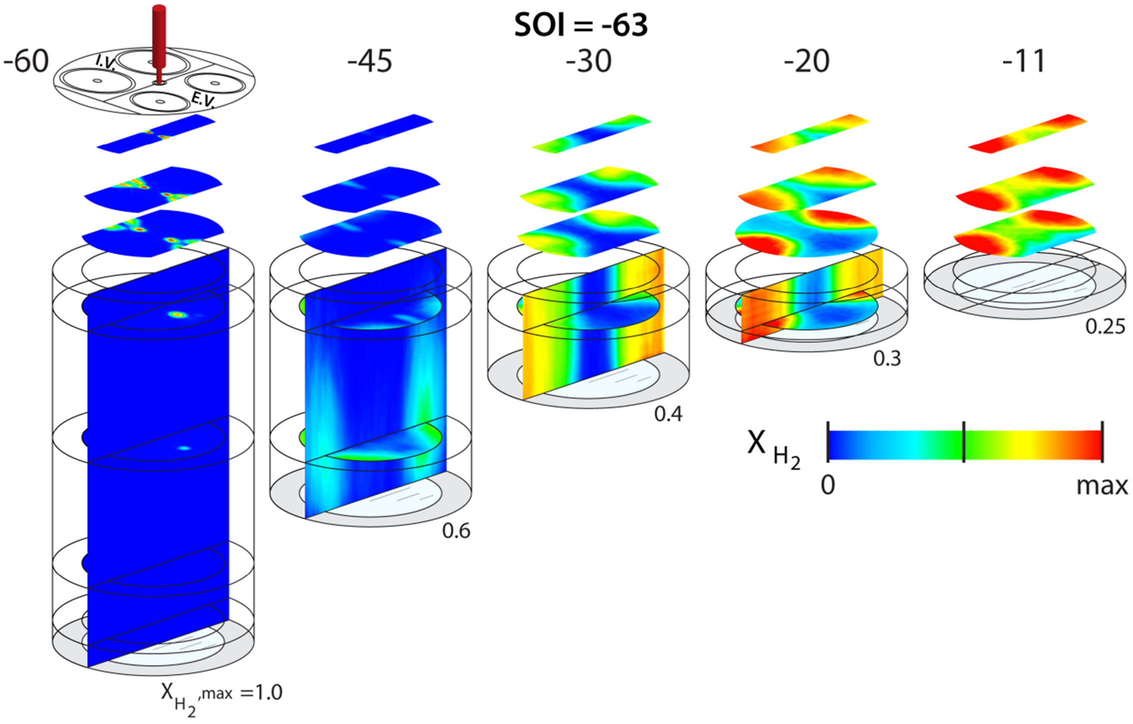

Figure 7.21: Fuel Distribution for SOI = 63° BTDC and β = 90°, horizontal and vertical planes. Images taken at 60, 45, 30, 20 and 11° BTDC. Metal engine testing done outside the scope of this work indicated this condition is close to the peak efficiency point of SOI = 70°.

Figures 7.22 and 7.23 show the fuel distribution at a SOI of 38° BTDC. The travel of the fuel at this condition is similar to that seen at SOI of 63°, but the stratification of the fuel is more exacerbated. At the ignition timing of 4° BTDC, the mole fraction is over 0.3 and fuel rich.

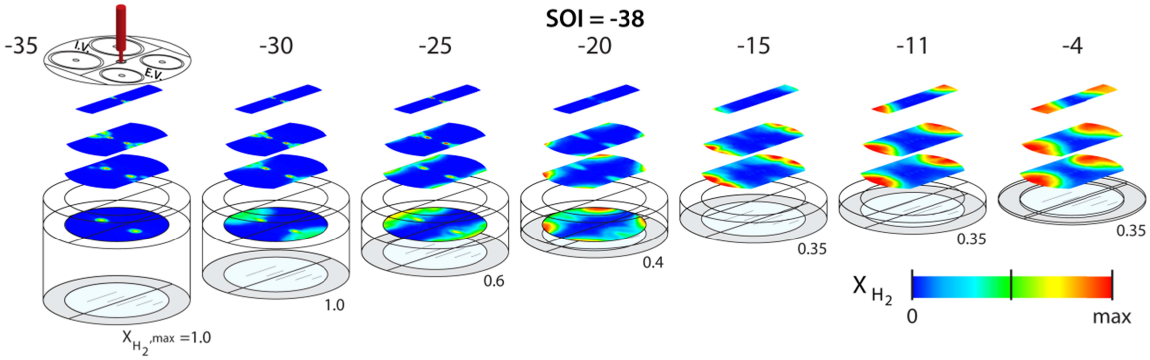

Figure 7.22: Fuel Distribution for SOI = 38° BTDC and β = 90°, horizontal planes only. Images taken at 35, 30, 25, 20, 15, 11, and 4° BTDC. Metal engine testing done outside the scope of this work indicated this condition has poor efficiency.

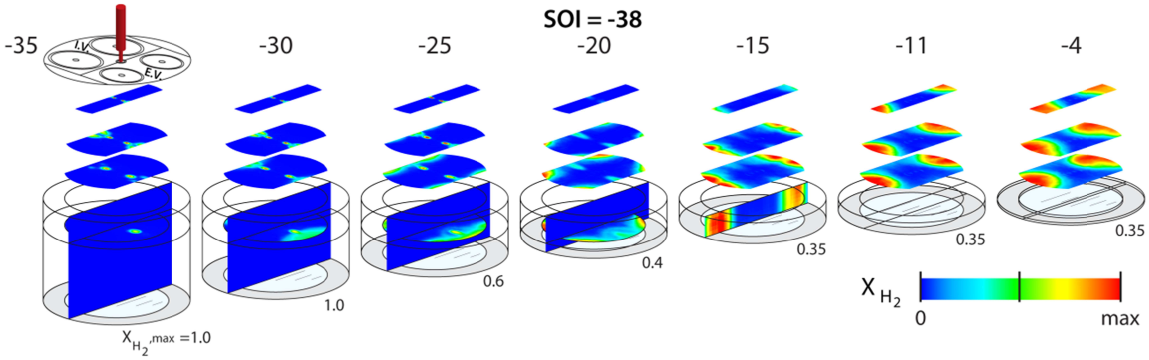

Figure 7.23: Fuel Distribution for SOI = 38° BTDC and β = 90°, horizontal and vertical planes. Images taken at 35, 30, 25, 20, 15, 11, and 4° BTDC. Metal engine testing done outside the scope of this work indicated this condition has poor efficiency.

7.4.3 Comparison of Fuel Distribution at Best Ignition Timing

Figures 7.24 and 7.25 compare the fuel distribution at the best ignition timing for the different SOI conditions. As noted previously, the best efficiency was found at β = 0° and an injection timing of 38° BTDC. This condition showed well mixed conditions of approximately ϕ=0.6 near the spark plugs, resulting in quick flame speeds without reaching very high temperatures. When the injection timing was set to 28°, the equivalence ratio near the spark plugs increased to approximately ϕ=1.0, which improves the flame speed slightly but also increases temperatures (and heat losses to the cylinder) dramatically. At SOI = 63°, the fuel is concentrated in the center of the combustion chamber, and at the local maxima of 90° the fuel distribution is relatively homogeneous throughout the imaged area.

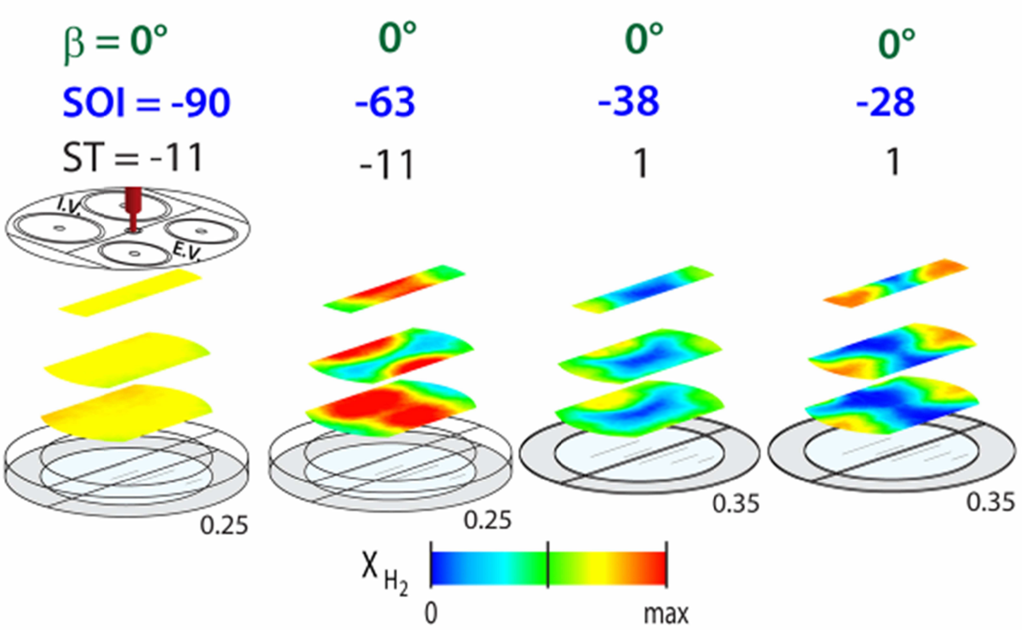

Figure 7.24: Fuel distribution for different injection timing (SOI) and best ignition timing (ST), β = 0°.

When β = 90° and SOI = 90° BTDC, the charge was relatively homogeneous. When the timing was reduced to SOI = 63° the charge is relatively rich near the spark plugs, and at 38° the charge is quite rich near the spark plugs. The engine efficiency would be optimized at or near the conditions shown for an injection timing of 63° BTDC.

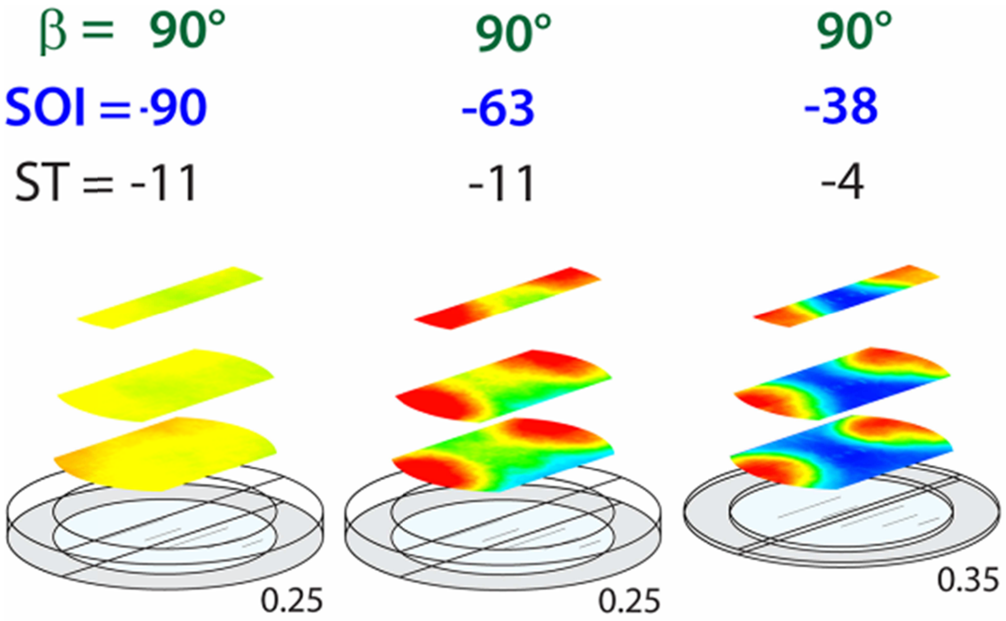

Figure 7.25: Fuel Distribution at best ignition timing, β = 90°.

7.4.4 Fuel Penetration

The vertical images were taken on a single crank angle degree resolution, and are shown in Figure 7.26 for β = 0^{o} and four SOI timings. The figures are ordered vertically, with each row of images representing an equivalent delay after SOI and as such can be compared directly. The influence of later injection is pronounced at 3° after SOI (87/60/35/25). At later injection timing the cylinder is at higher pressure, and the penetration distance of the fuel from the injector is dramatically reduced. The higher pressure also influences the spread of the injection jets. The later images at earlier injections show the interaction of the exterior jets on the center jet, and as such a larger Coanda effect is certainly plausible at the earlier SOIs.

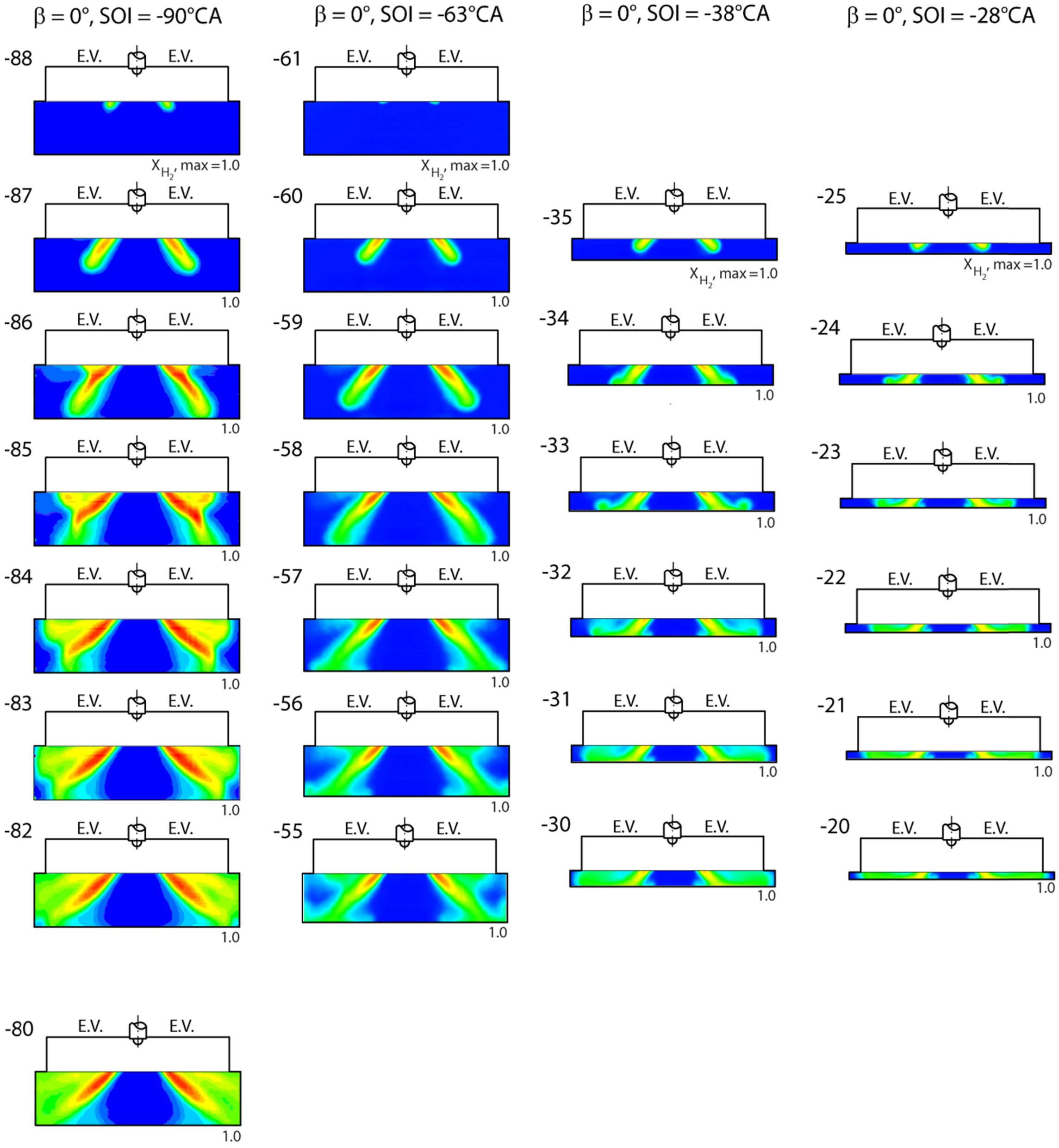

Figure 7.26: Fuel Distribution Immediately following Injection, Four Injection Timings.

7.4.5 Vertical Imaging: β = 0° and β = 90°

A summary of all vertical images for SOI = 90° is shown in Figure 7.27. In figures 7.9, 7.10, 7.17 and 7.18 the fuel distribution was shown to be relatively homogeneous for both injector orientations. Figure 7.27 indicates that the path the fuel takes to achieve that homogeneity is quite different for the two injector orientations.

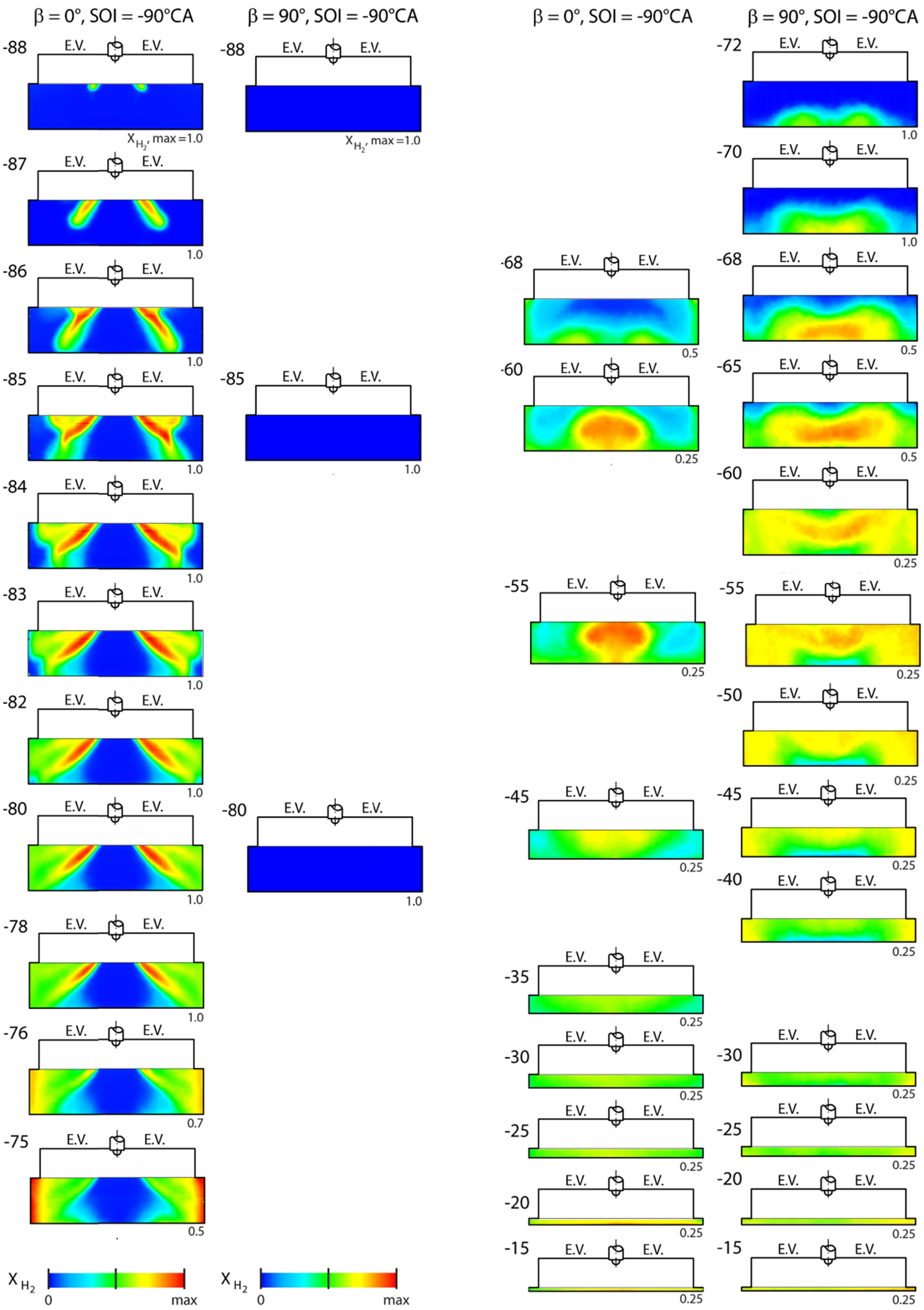

Figure 7.27: Vertical Imaging for β = 0° and β = 90°, SOI = 90°.

The equivalent vertical imaging for a SOI at 63° is shown in Figure 7.28. Near the ignition timing, the fuel distribution was rich near the center for the β = 0° case, and was rich near the edges for the β = 90° case.

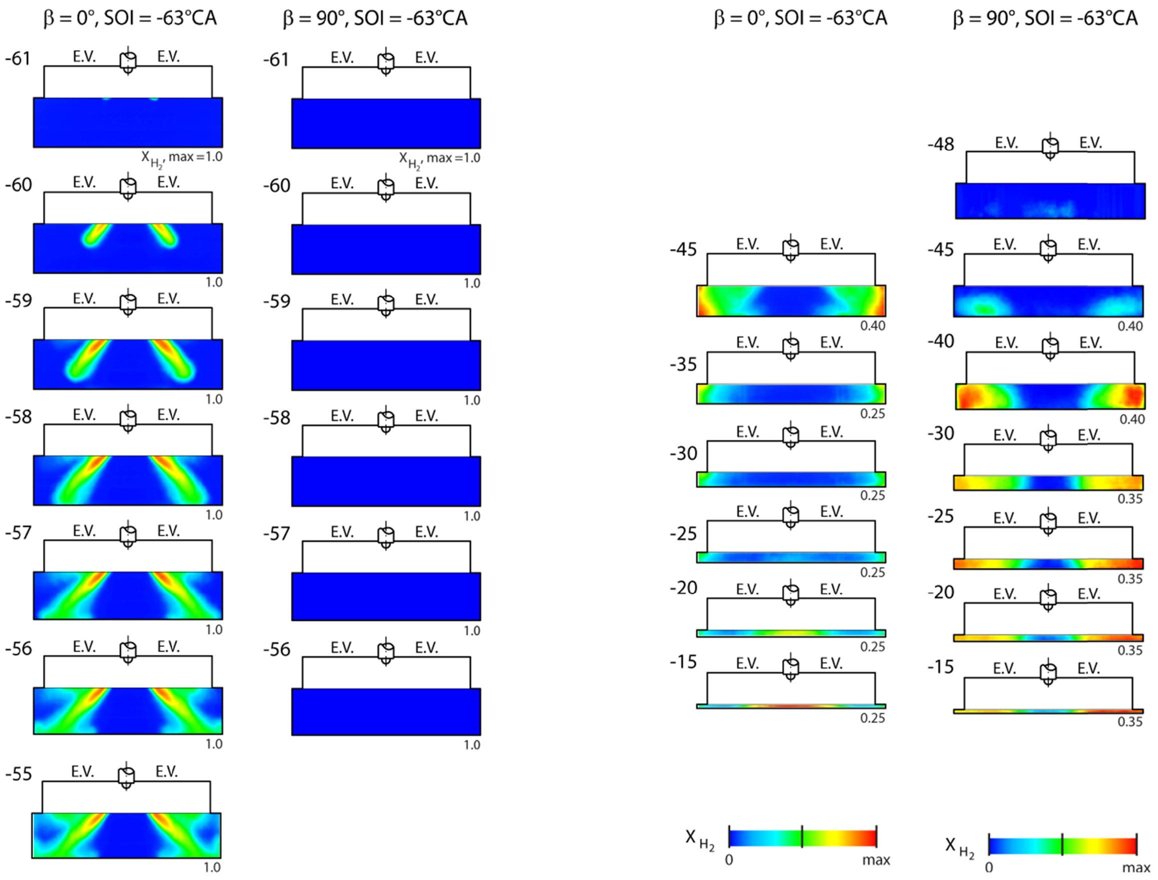

Figure 7.28: Vertical Imaging for β = 0° and β = 90°, SOI = 63°.

The vertical imaging for a SOI at 38° is shown in Figure 7.29. At this condition, vertical imaging was not possible with any fidelity near the ignition timing of 1° ATDC and 4° BTDC for the β = 0° and β = 90° conditions, respectively. Nevertheless, at the last condition for which vertical imaging was attempted, rich zones were found at the edges of the image, as close to the spark plugs as could be measured.

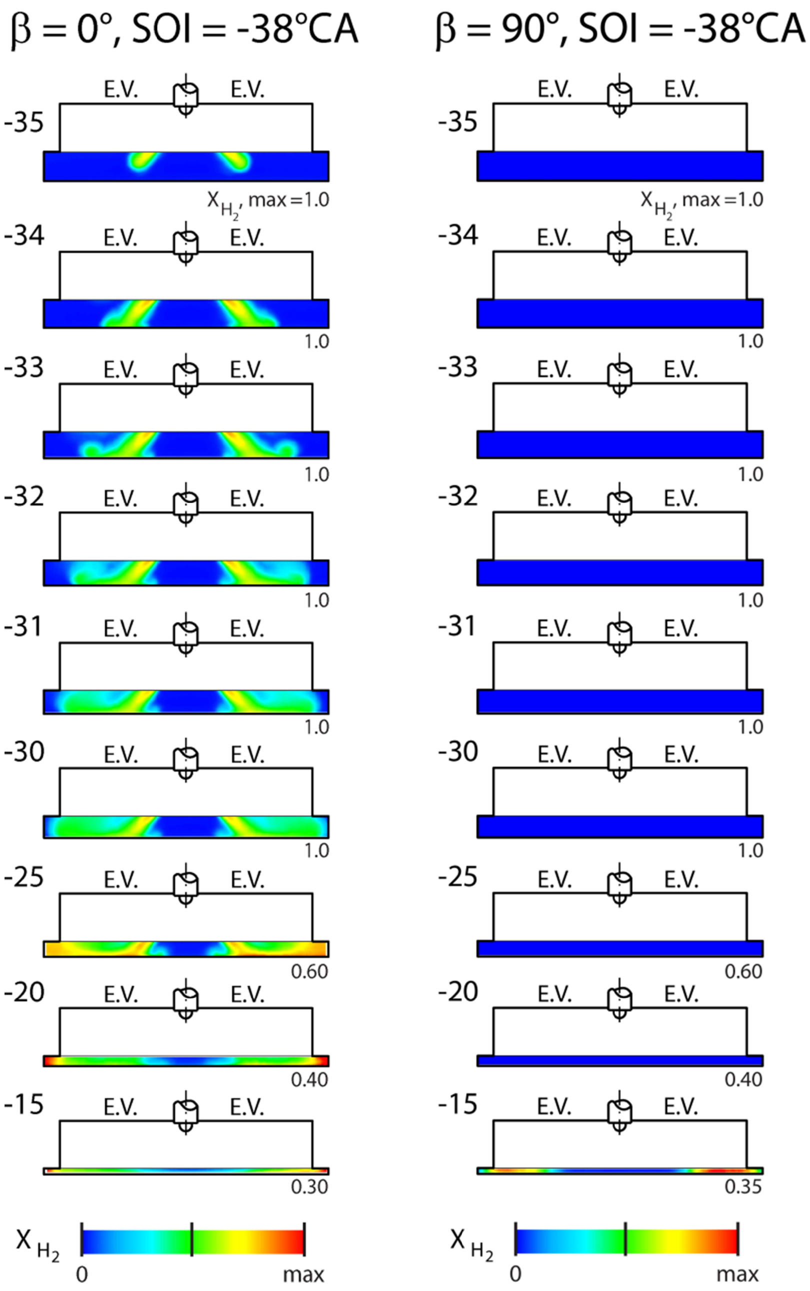

Figure 7.29: Vertical Imaging for β = 0° and β = 90°, SOI = 38°.

The vertical imaging for a SOI at 28° is shown in Figure 7.30. Again, at this condition vertical imaging was not practicable near the ignition timing of 1° ATDC. At the last condition for which vertical imaging was attempted, rich zones were found at the edges of the image, as close to the spark plugs as could be measured.

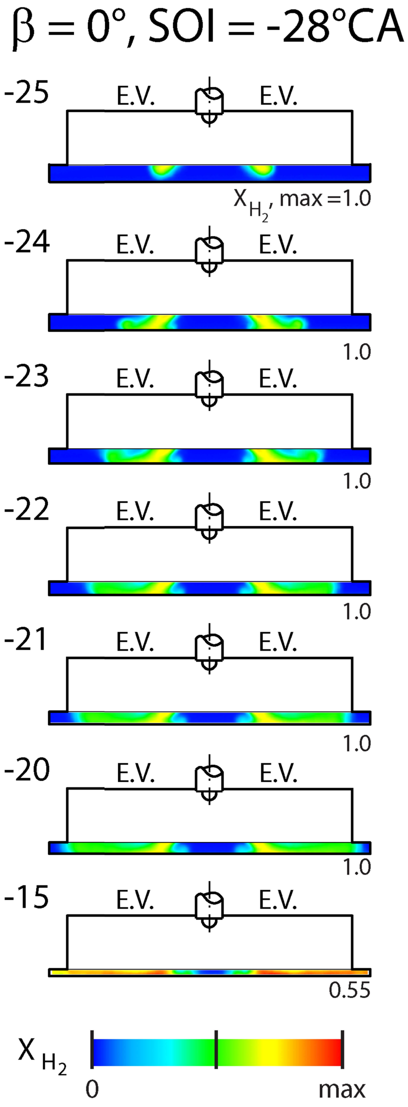

Figure 7.30: Vertical Imaging for β = 0° and SOI = 28°.

7.4.6 RMS and Mean Molar Fraction, Highest Horizontal Plane

In order to determine the magnitude of cycle to cycle fluctuations of fuel distributions, the RMS of the fuel distribution was generated for all images. Perhaps most critical is the fuel distribution nearest the ignition locations, i.e. the highest of the horizontal planes. Figures 7.31 and 7.32 show the images that correspond to the ignition timings of the $\beta = 0°$ and $\beta = 90°$ cases, respectively. As can be seen, all of these cases show relatively little fluctuation in the areas closest to the ignition location. All of the fuel mole fraction images in this section are scaled to a common maximum molar fraction of 0.35, and all of the RMS images in this section are scaled to a common mole fraction of approximately 0.14.

The fuel distribution is relatively homogeneous when the SOI is 90°, regardless of whether $\beta = 0°$ or $\beta = 90°$. The fuel distribution for $\beta = 0°$ and SOI = 38° is somewhat similar to the distribution seen at $\beta = 90°$ and SOI = 63°. The fuel distribution that can be seen at $\beta = 0°$ and SOI = 28° is somewhat similar to the distribution seen at $\beta = 90°$ and SOI = 38°.

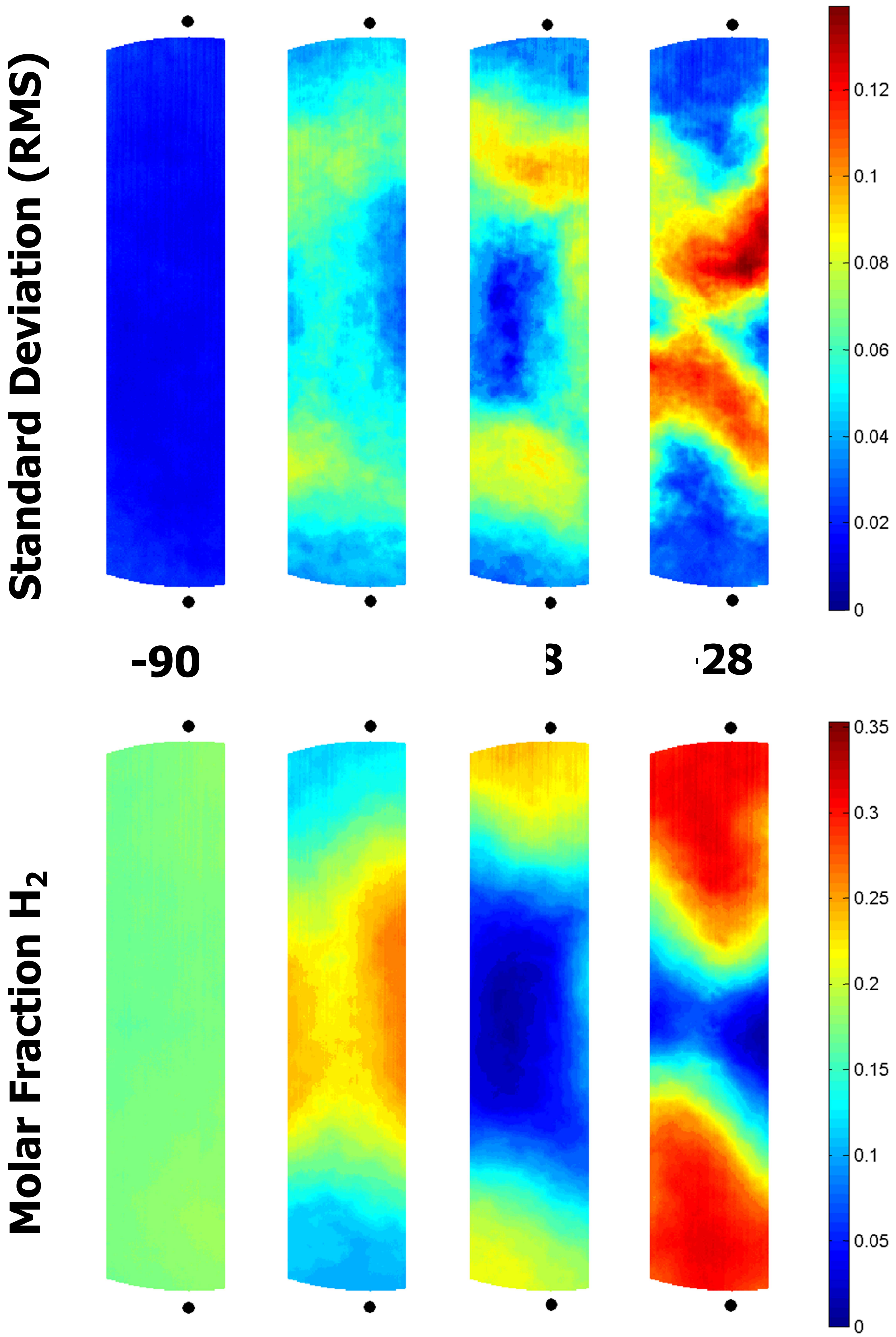

Figure 7.31: Standard Deviation of measurement and fuel mole fraction for four injection timings at their respective ignition timings, β = 0°. The centers of the spark plugs are indicated by black dots.

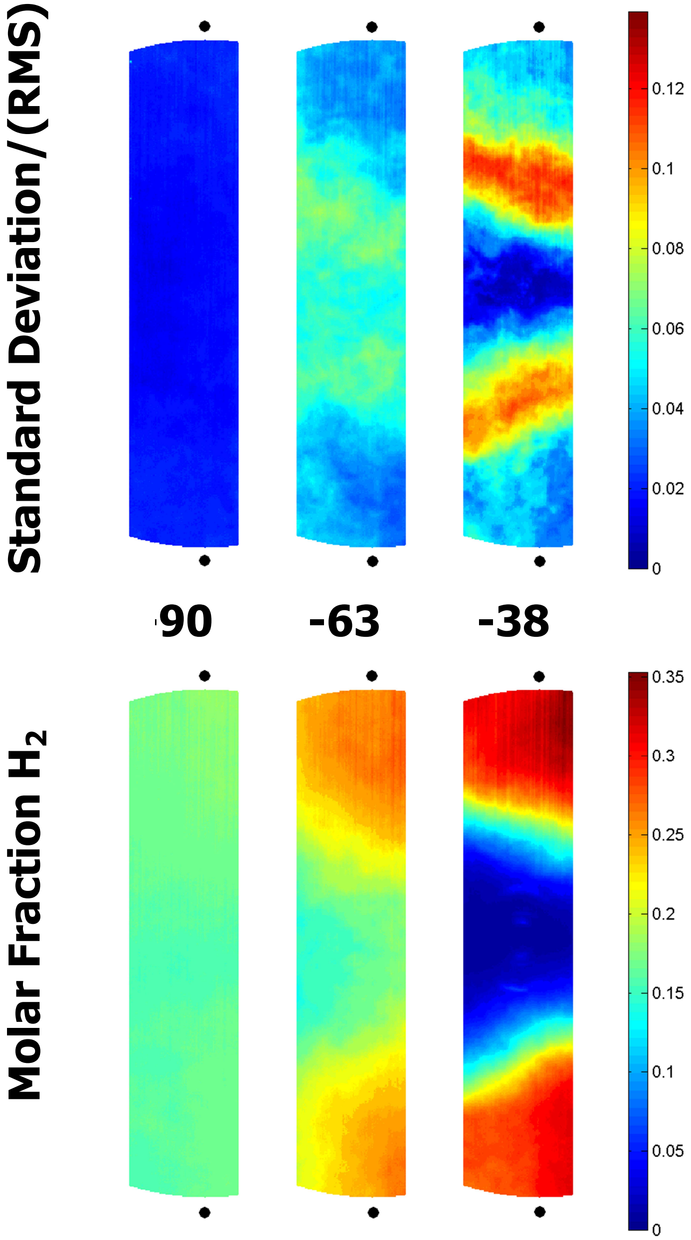

Figure 7.32: Standard Deviation of measurement and Molar Fraction for four injection timings at their respective ignition timings, β = 90°. The centers of the spark plugs are indicated by black dots.

7.4.7 RMS and Mean Mole Fraction near the ignition location

As was previously mentioned, with the current engine setup the view into the cylinder was cropped in both vertical and horizontal images. As such we could not characterize the fuel distribution at the exact ignition location.

Nevertheless, it is still possible to analyze the fuel distribution 'near' the ignition location. To that end, the 250 pixels closest to the spark plugs were taken as an indicator of fuel distribution at the ignition location. These pixels are highlighted in Figure 7.33. The "near ignition" locations are roughly 5 to 8 mm from the center of the spark plug gap. As such, the average fuel distribution near the spark plug in these locations cannot be considered a conclusive indicator of the fuel distribution at the ignition location for fuel distributions which are quite spatially dependent, but the data still provide relevant information on fuel mixing.

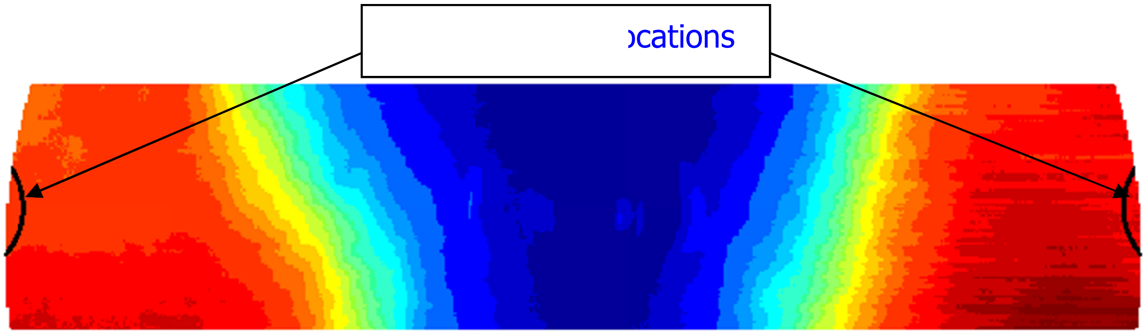

Figure 7.33: Area Defined as 'Near Ignition' in this Section.

The values for equivalence ratio and RMS were analyzed for the near ignition locations for the different injection times and β = 0°. The near-ignition equivalence ratio (near spark) and standard deviation of equivalence ratio are shown in Figure 7.34. The corresponding metal engine data for indicated thermal efficiency and combustion stability (represented as the COV of IMEP) are also provided in the figure.

At SOI of 90°, the average fuel distribution near the ignition sites was similar to the global mole fraction of 0.144 (equivalence ratio 0.4), and the RMS mole fraction is quite low. The metal engine experiment shows stable combustion but relative low performance. At a SOI of 63°, the average fuel distribution near the ignition sites was quite low compared to global fuel distribution. Moreover, the RMS of molar fraction was high. Correspondingly, the indicated thermal efficiency was low and the combustion was not stable.

At SOI of 38°, the average fuel distribution near the ignition sites was 0.22, which is moderately high compared to global fuel distribution. Even though the RMS of molar fraction was high, the combustion was quite stable in the metal engine and the indicated efficiency was quite high. Temperatures in the cylinder are likely to remain low; the adiabatic flame temperature at a molar fraction of 0.22 is roughly 1900K; furthermore, the areas analyzed outside the near-ignition sites have low molar fractions as well.

At SOI of 28°, the average fuel distribution near the ignition sites was stoichiometric, which is quite high compared to global fuel distribution. The RMS of mole fraction was reduced compared to the distribution seen at a SOI of 38°. The combustion stability seen on the metal engine was quite stable. However, the overall efficiency seen on the metal engine was quite low. Temperatures in the cylinder are likely to be high; for reference, adiabatic flame temperature at stoichiometry is roughly 2400K. Exacerbating this problem is the large zones of stratified near-stoichiometric charge that will likely be further compressed by burned gases before combustion, raising the temperatures further.

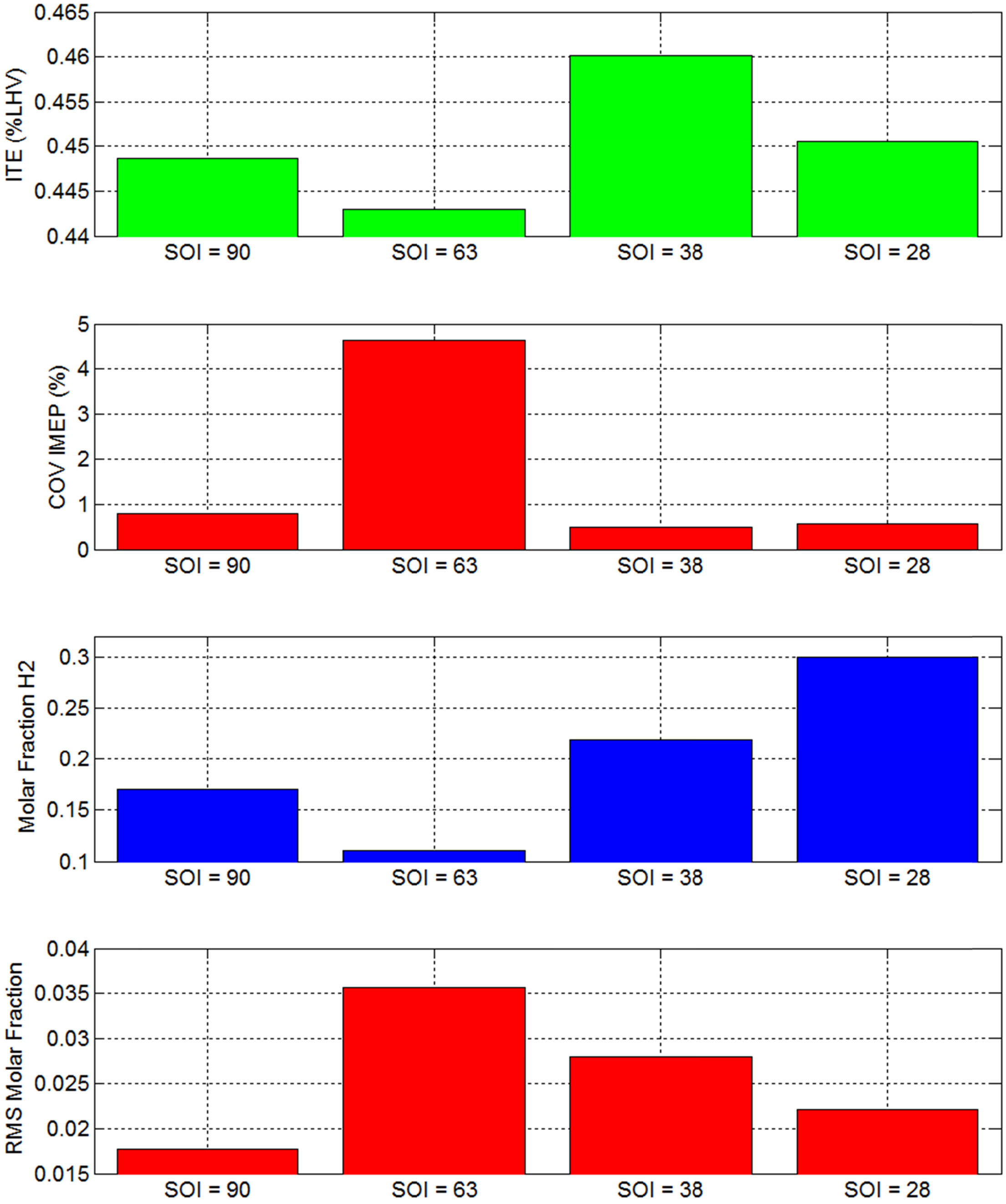

Figure 7.34: Pertinent Metal Engine Statistics and Optical Engine Near-Spark Data for β = 0°.

7.4.8 Repeatability

In order to determine the repeatability of the measurements, 26 vertical images were repeated on separate occasions. The results are shown in Figures 7.35 and 7.36, and demonstrate high levels of qualitative and quantitative repeatability.

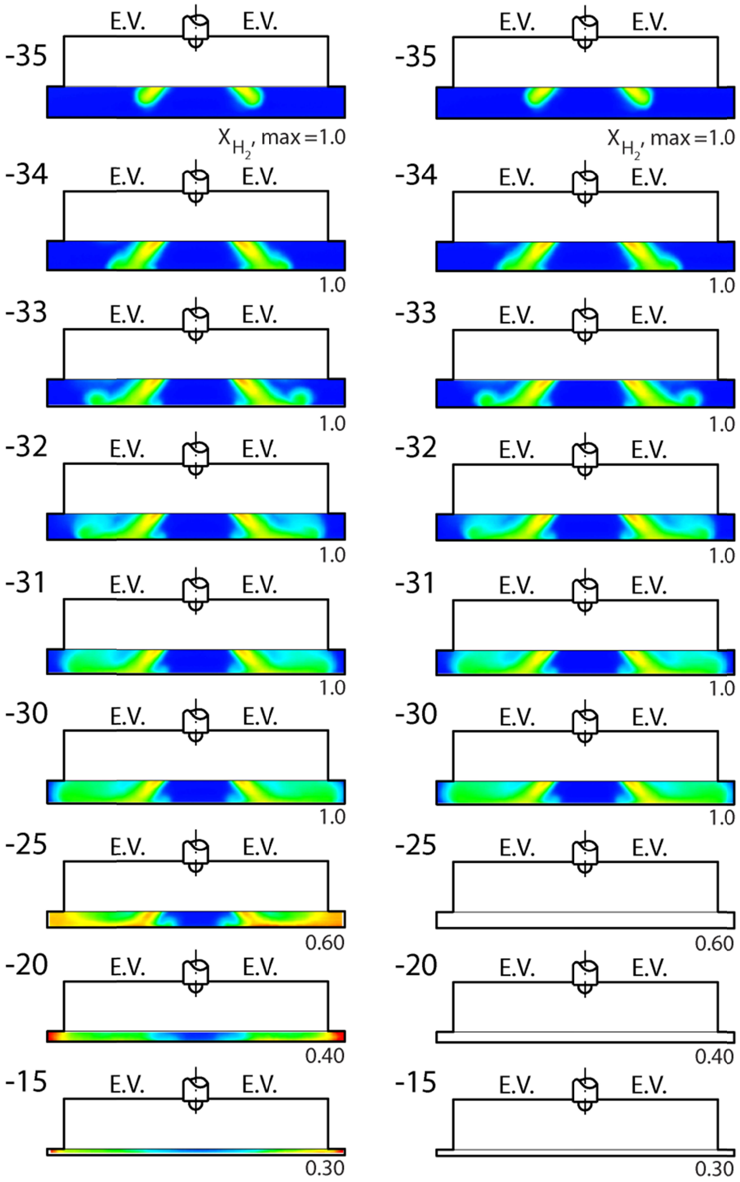

Figure 7.35: Repeatability, Vertical Images at SOI = 38°.

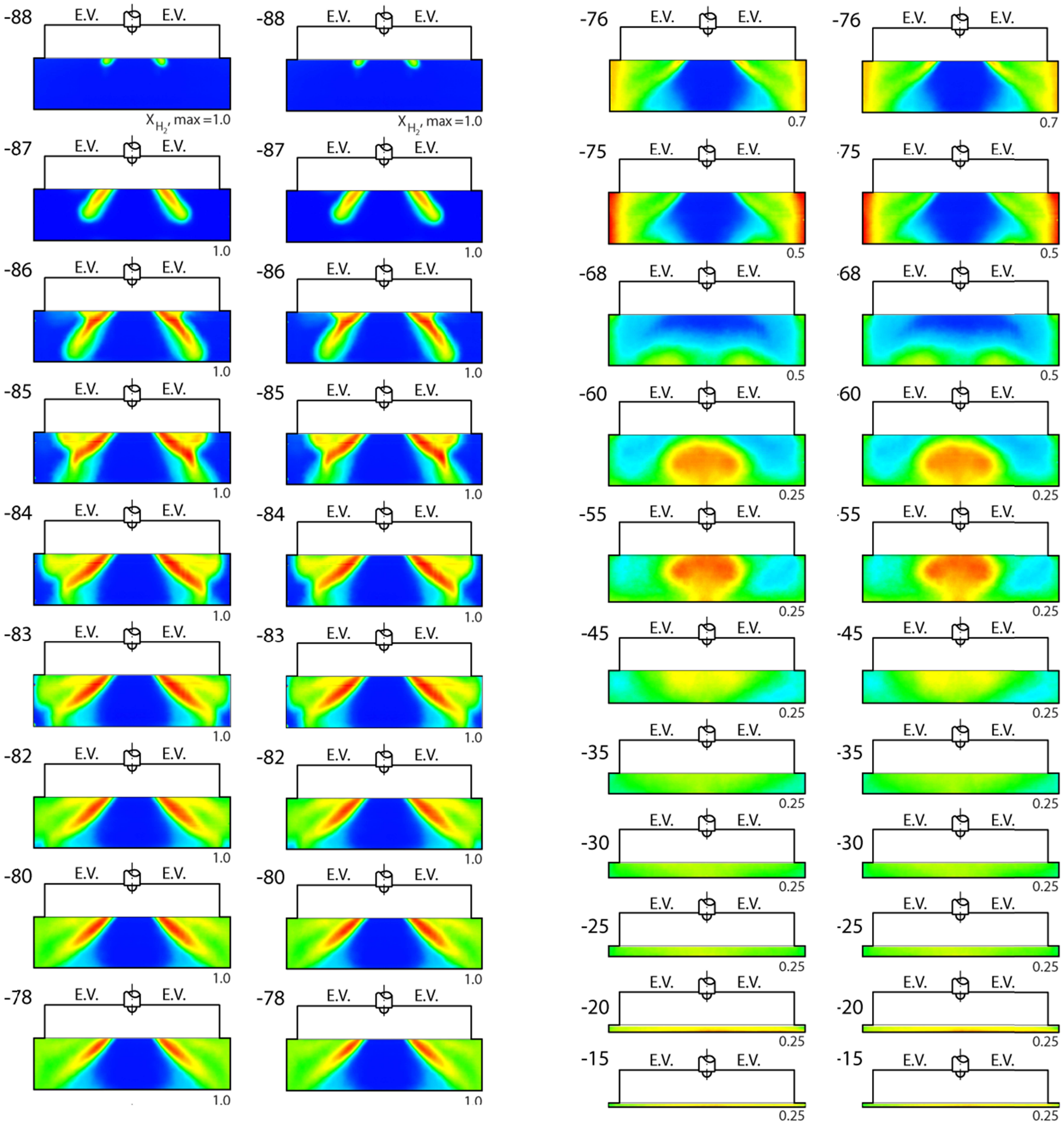

Figure 7.36: Repeatability, Vertical Images at SOI = 90°.

7.5 Conclusions

The fuel distribution of a high-efficiency hydrogen combustion system was characterized for a total of 255 variations of injector nozzle orientation, injection timing, imaging timing, and image plane. At β =0°, the most efficient operating point of SOI = 38° was shown to have well mixed, but relatively rich zones near the spark plugs. A relatively poor injection timing (in terms of metal engine performance) of SOI = 63° showed a rich zone in the center of the combustion chamber, away from the spark plugs, explaining the long burn duration and poor combustion stability of the corresponding metal engine testing. A SOI of 90° yielded near-homogeneous fuel distribution, and the overall efficiency for SOI = 90^{o} was between the two extremes in performance and image characteristics of SOI – 38^{o} and 63^{o}. At a SOI of 28°, the mixture near the spark plugs was slightly richer than stoichiometric. The high flame temperatures that would result from this rich mixture explain the high heat release rates, high NOx emissions, and presumably large amount of heat transferred to the cylinder walls.

Metal engine experiments were not conducted at Ford or Sandia at 1500 RPM with a nozzle orientation of β = 90°. The optical engine results suggest that the near-homogenous condition at 90° SOI would perform in roughly an equivalent manner to the near-homogenous β =0° and 90° SOI. At a SOI of 38°, the fuel distribution is similar to that at β =0° and a SOI of 28°; in other words, with too much stratification for efficient operation. At a SOI of 63°, the fuel distribution is similar to that at β =0° and a SOI of 38°; and is anticipated to produce efficient operation.

The cylinder heads that were used in the metal and optical engine experiments were designed with the anticipation, based on prior work, that the low quench distance and high flame speeds of hydrogen would make a large amount of charge motion unnecessary and potentially undesirable. While beyond the scope of this work, experiments which enhance mixing, heat transfer, and turbulence/chemistry interactions through increased swirl and tumble have academic value towards understanding the fundamental mechanisms important in hydrogen combustion systems. This would be a good area for future metal and optical engine studies.

In summary, the imaging results indicate similar performance can be achieved using either fuel injector orientation. In general, a fuel distribution should be characterized by a well-mixed charge near the ignition location of approximately 0.6 phi. When the charge is relatively homogeneous globally, burn durations are too long, and when the local equivalence ratio exceeds 0.8 phi, temperatures rise rapidly and heat transfer to the cylinder walls becomes high.

Chapter 8

Summary, Conclusions, and Future Work

8.1 Summary

There are many means to increase the efficiency of any engine, and the advantageous properties of hydrogen, particularly the wide flammability limits and the sensitivity of flame speed to equivalence ratio, allow for a greater range of freedom compared to conventional fuels. In this study, a large parametric space was explored and many experiments were conducted to characterize methods to improve system efficiencies for a hydrogen internal combustion engine. Direct improvement of combustion efficiency and indirect methods such as minimizing NOx, increasing engine load, and decreasing engine friction and pumping losses were explored and characterized using quantitative metrics.

In general, for premixed fuel distributions, the highest thermal efficiencies were observed for $\phi \cong 0.4$. Net indicated thermal efficiency (ITE) increased by about 0.3% of the lower heating value (LHV) of hydrogen (0.7% relative improvement) per 1000 RPM for engine speeds in the range of 2000-4000 rpm. A smaller bore to stroke ratio (B/S = 0.94 compared to 1.13) improved efficiency by 2% of LHV (4.5% relative improvement). Increasing manifold pressure at $\phi = 0.4$ improved gross indicated efficiency by 0.2% of LHV per bar of net indicated mean effective pressure (IMEP, 0.45% relative improvement) over the range of intake pressures tested (from 0.35 to 2 bar). A compression ratio of CR = 13.7:1 was close to optimum from a brake thermal efficiency standpoint, and improved net ITE by 1.3% (3% relative improvement).

The best direct injection designs, like the 5H and 3+3H injectors, improved efficiency by 1.4% and 1.7% of LHV, respectively, compared to pre-mixed operation. When combined with a dual-side ignition cylinder head, efficiency improved by another 0.9%. Best performance of the H_2 engine designs considered in this study was 47.7% Net ITE and was achieved using the 3+3 fuel injector at 12.5:1 CR, at 3000 RPM, with 100 kPa manifold pressure, yielding 200 ppm of NO_x emissions. With a slightly earlier injection timing, efficiency decreased by 0.1%, but NOx decreased from 200 ppm to 60 ppm. Efficiency is anticipated to increase further with higher manifold pressures and higher compression ratios.

The fuel distribution produced by the 3+3 was characterized using an optically accessible engine. The conditions that corresponded to the highest efficiency resulted in mixtures near the ignition location(s) with an equivalence ratio of about $\phi = 0.6$. This was true for both fuel injector orientations ($\beta = 0^o$ and $\beta = 90^o$), and for both central ignition and dual-side ignition cylinder heads.

The ability of water injection to improve NOx emissions was tested, both on a port injection (PI) fueled engine and a direct injection (DI) fueled engine. The PI fueled engine, coupled with DI water injection, reduced NOx emissions by 85% without a penalty in fuel consumption. The DI fueled engine, coupled with PI water, reduced NOx emissions by 87% with only a 2% fuel consumption penalty; exceeding the performance of multiple injection strategies.

8.2 Conclusions

Detailed conclusions have been provided in the corresponding chapters of the thesis. Three critical outcomes of the work are summarized here.

1. Hydrogen IC engine strategies must use stratification of lean fuel/air mixtures to optimize engine performance. Fuel air charges which were

relatively homogeneous globally produced burn durations which were too long, and when the local equivalence ratio exceeded $\phi = 0.8$, temperatures in the cylinder increased, producing unacceptable levels of NOx and poor efficiency. Global equivalence ratios of $\phi = 0.4$, with local equivalence ratio near the ignition location of $\phi = 0.6$, produced the highest efficiencies observed. Fuel injector nozzle design clearly had large impact on stratification, and there were multiple fuel injector tip geometries that achieved advantageous stratification conditions.

2. Water injection strategies were very effective at reducing NOx emissions with small penalties in fuel consumption. The injection of water into the intake charge (PI H_2O injection) of a DI H_2 engine decreased NO_x emissions by 87%. The injection of water into the combustion cylinder (DI H_2O injection) of a PI H_2 engine decreased NO_x emissions by 95%.
3. The best hydrogen engine net indicated thermal efficiency demonstrated in this work was 47.7%. Although the ITE is quite high, the penalties of converting methane to hydrogen (both in terms of economic costs and energy losses) are likely to make such a conversion unwarranted for ground transportation purposes based on the high efficiency alone. However, other factors drive research and application of hydrogen engine technology. For example, tailpipe CO_2 emissions are near-zero for H_2 engines; production methods for hydrogen could change and eliminate methane as the primary source of hydrogen, and hydrogen engine technology can (and is) being applied to weight-critical aerospace applications.

The intent of the work was to evaluate the mechanisms and methods of improving the efficiency of a hydrogen internal combustion engine and to quantify the engine response to such changes. Many methods were evaluated, including varying the:

1. Compression Ratio,
2. Engine Speed,
3. Manifold Pressure,
4. Equivalence Ratio,
5. Amount, location, and phasing of water injection,
6. Phasing of fuel injection timing
7. Design of injector nozzle pattern, and
8. Location/Number of Ignition Sites

As expected, all these parameters had significant impact on the overall efficiency of the engine. In total, the results indicate that compression ratios near 14:1 optimize the tradeoff between fundamental thermodynamic advantages and mechanical friction disadvantages. Increases in engine speed improve the net thermal efficiency substantially, but come with a commensurate friction loss as well. Increased manifold pressure in a manner simulating turbocharging improved efficiency at the conditions tested. No knock limit or other practical limit was found. Equivalence ratio was optimized at $\Phi = 0.4$. Water injection allowed the overall load limit of a NO_x-regulated engine to increase by up to 26.7%, depending upon assumptions. In terms of combustion chamber design, the interaction between nozzle design, injection timing, and ignition location was found to be critical.

8.3 Future Work

This work has done much to document and analyze the efficiency benefits of H_2 engines and how to successfully achieve those benefits over the wide range of operating conditions expected in IC engine applications. This work also points towards how more efficiency benefits can be gained. For example, the 3+3 injector yielded very good efficiency at compression ratios close to 12:1. The analysis indicated that a gain of 1% ITE should be quite feasible at a compression ratio of about 14:1. Similarly, water injection was never combined with the 3+3 injector. As the fuel distribution is now known from the results of the optical engine studies, the nozzles of the water injector could be used to selectively cool areas presumed to burn at higher temperatures, reducing NOx emissions. Finally, simulated turbocharging was found to improve absolute efficiency, and when combined with a smaller engine design, would minimize engine pumping or sub-optimal cam phasing. No experiments were conducted combining the best of all of these attributes, which may diminish the overall returns. A wide map of engine performance with the presumed optimal design would be useful to evaluate the viability of a hydrogen engine for a given application.

Design changes not considered in this work may further improve efficiency substantially. Hydrogen engines are well disposed to utilize bottoming cycles; the fuel is expensive, the engines are not anticipated to require aftertreatment, and the Nusselt, Prandtl, and Reynolds numbers of the exhaust are generally favorable in terms of heat extraction when compared to gasoline engines. These advantages may be able to overcome the disadvantage (compared to gasoline engines) of low temperature exhaust. Insulated pistons and cylinder heads could transfer more energy into the piston and the exhaust facilitating bottoming cycles and further efficiency gains.

Of late, the attention of industry for gaseous fuels has focused on natural gas. As the designs presented in this document represent some of the highest efficiencies known in automotive-sized engines, some questions as to the applicability of similar designs to compressed natural gas (CNG) or methane are inevitable. Unfortunately, methane has inferior properties compared to hydrogen, particularly in terms of the sensitivity and response between equivalence ratio and flame speed. Some advantages might be found in certain stratified conditions that otherwise would not be operable, but large gains in maximum efficiency are not anticipated from the 3+3 injector operating with methane. Of course, the overall engine efficiency would improve based on the dual-ignition cylinder head alone. Further, it is unlikely that a dual CNG + H_2 system would be economically feasible for transportation applications in the near term. Nevertheless, designs that use the 3+3 injector to preferentially stratify hydrogen near the ignition locations in a premixed methane/air mixture would likely be quite efficient and research on the system certainly would be both worthwhile and enlightening.

APPENDIX

Appendix A Injectors/Combustion Chamber/Tests Conducted Matrix

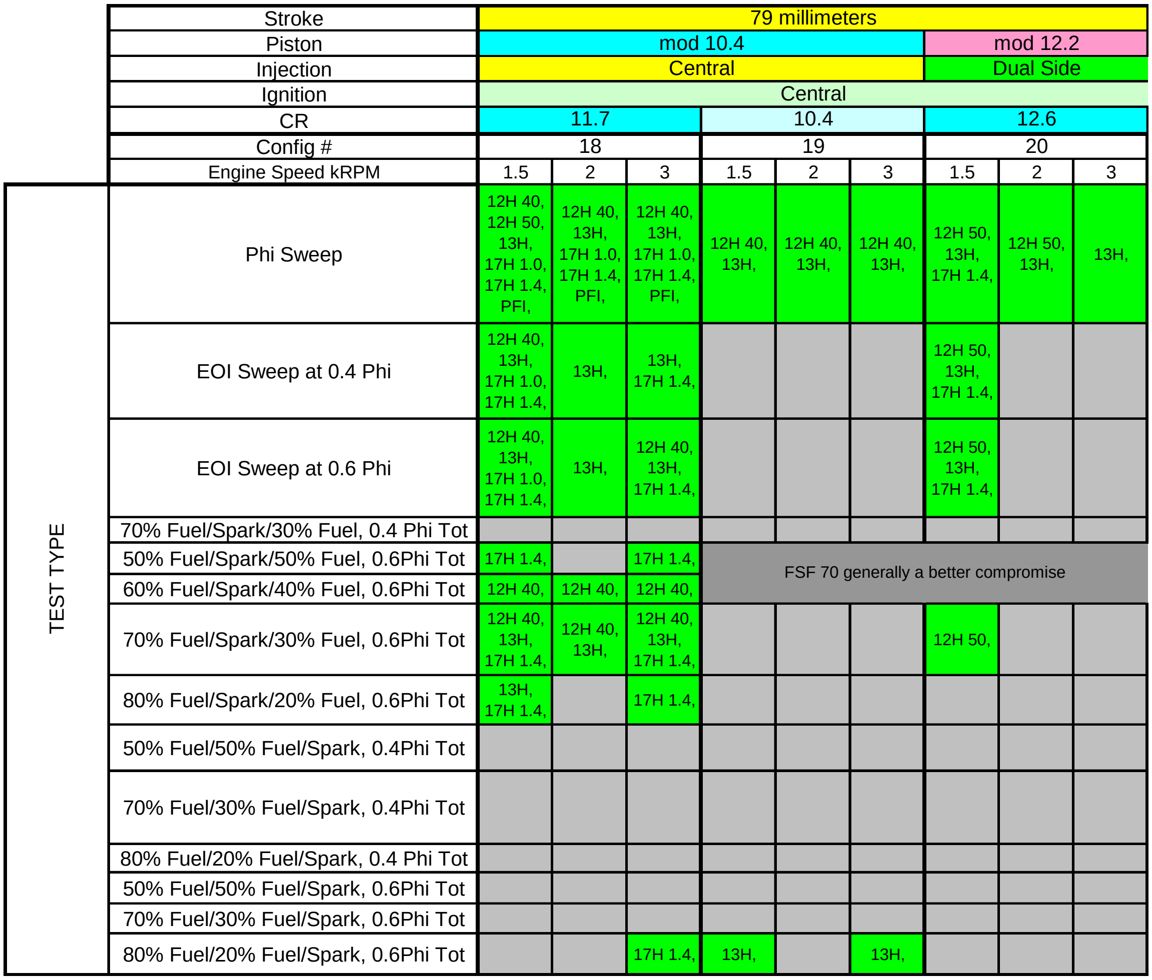

	Stroke	79 millimeters								
	Piston	mod 10.4						mod 12.2		
	Injection	Central						Dual Side		
	Ignition	Central								
	CR	11.7			10.4			12.6		
	Config #	18			19			20		
	Engine Speed kRPM	1.5	2	3	1.5	2	3	1.5	2	3
TEST TYPE	Phi Sweep	12H 40, 12H 50, 13H, 17H 1.0, 17H 1.4, PFI,	12H 40, 13H, 17H 1.0, 17H 1.4, PFI,	12H 40, 13H, 17H 1.0, 17H 1.4, PFI,	12H 40, 13H,	12H 40, 13H,	12H 40, 13H,	12H 50, 13H, 17H 1.4,	12H 50, 13H,	13H,
	EOI Sweep at 0.4 Phi	12H 40, 13H, 17H 1.0, 17H 1.4,	13H,	13H, 17H 1.4,				12H 50, 13H, 17H 1.4,		
	EOI Sweep at 0.6 Phi	12H 40, 13H, 17H 1.0, 17H 1.4,	13H,	12H 40, 13H, 17H 1.4,				12H 50, 13H, 17H 1.4,		
	70% Fuel/Spark/30% Fuel, 0.4 Phi Tot									
	50% Fuel/Spark/50% Fuel, 0.6Phi Tot	17H 1.4,		17H 1.4,	FSF 70 generally a better compromise					
	60% Fuel/Spark/40% Fuel, 0.6Phi Tot	12H 40,	12H 40,	12H 40,						
	70% Fuel/Spark/30% Fuel, 0.6Phi Tot	12H 40, 13H, 17H 1.4,	12H 40, 13H,	12H 40, 13H, 17H 1.4,				12H 50,		
	80% Fuel/Spark/20% Fuel, 0.6Phi Tot	13H, 17H 1.4,		17H 1.4,						
	50% Fuel/50% Fuel/Spark, 0.4Phi Tot									
	70% Fuel/30% Fuel/Spark, 0.4Phi Tot									
	80% Fuel/20% Fuel/Spark, 0.4 Phi Tot									
	50% Fuel/50% Fuel/Spark, 0.6Phi Tot									
	70% Fuel/30% Fuel/Spark, 0.6Phi Tot									
	80% Fuel/20% Fuel/Spark, 0.6Phi Tot			17H 1.4,	13H,		13H,			

Figure A.1: Injectors/Combustion Chamber/Tests Conducted, part 1.

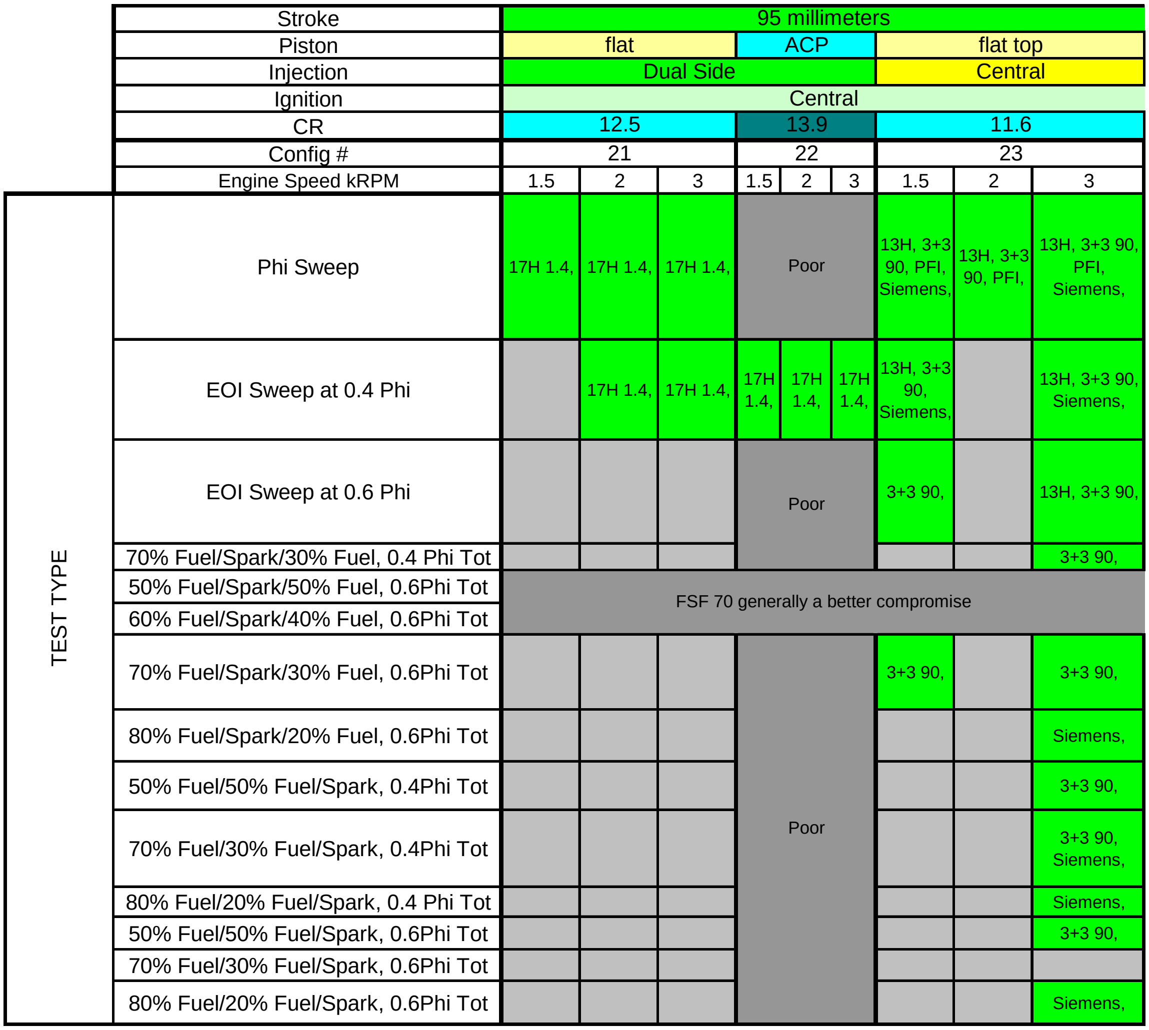

	Stroke	95 millimeters								
	Piston	flat			ACP			flat top		
	Injection	Dual Side						Central		
	Ignition	Central								
	CR	12.5			13.9			11.6		
	Config #	21			22			23		
	Engine Speed kRPM	1.5	2	3	1.5	2	3	1.5	2	3
TEST TYPE	Phi Sweep	17H 1.4,	17H 1.4,	17H 1.4,	Poor			13H, 3+3 90, PFI, Siemens,	13H, 3+3 90, PFI,	13H, 3+3 90, PFI, Siemens,
	EOI Sweep at 0.4 Phi		17H 1.4,	17H 1.4,	17H 1.4,	17H 1.4,	17H 1.4,	13H, 3+3 90, Siemens,		13H, 3+3 90, Siemens,
	EOI Sweep at 0.6 Phi				Poor			3+3 90,		13H, 3+3 90,
	70% Fuel/Spark/30% Fuel, 0.4 Phi Tot									3+3 90,
	50% Fuel/Spark/50% Fuel, 0.6Phi Tot	FSF 70 generally a better compromise								
	60% Fuel/Spark/40% Fuel, 0.6Phi Tot									
	70% Fuel/Spark/30% Fuel, 0.6Phi Tot				Poor			3+3 90,		3+3 90,
	80% Fuel/Spark/20% Fuel, 0.6Phi Tot									Siemens,
	50% Fuel/50% Fuel/Spark, 0.4Phi Tot									3+3 90,
	70% Fuel/30% Fuel/Spark, 0.4Phi Tot									3+3 90, Siemens,
	80% Fuel/20% Fuel/Spark, 0.4 Phi Tot									Siemens,
	50% Fuel/50% Fuel/Spark, 0.6Phi Tot									3+3 90,
	70% Fuel/30% Fuel/Spark, 0.6Phi Tot									
	80% Fuel/20% Fuel/Spark, 0.6Phi Tot									Siemens,

Figure A.2: Injectors/Combustion Chamber/Tests Conducted, part 2.

	Stroke	95 millimeters								
	Piston	Wendy			MACP					
	Injection	Dual Side								
	Ignition	Central								
	CR	12.5			13.4			11.4		
	Config #	24			25			26		
	Engine Speed kRPM	1.5	2	3	1.5	2	3	1.5	2	3
TEST TYPE	Phi Sweep	13H, 17H 1.4, 3+3 90,	13H, 17H 1.4, 3+3 90,	13H, 17H 1.4, 3+3 90,	13H, 17H 1.4, 3+3 90,	13H, 17H 1.4, 3+3 90,	13H, 17H 1.4, 3+3 90,	13H, 17H 1.4,	13H, 17H 1.4,	13H, 17H 1.4,
	EOI Sweep at 0.4 Phi	13H, 17H 1.4, 3+3 90,		13H, 17H 1.4, 3+3 90,	13H,		13H,	17H 1.4,		13H, 17H 1.4,
	EOI Sweep at 0.6 Phi	13H, 17H 1.4, 3+3 90,		13H, 17H 1.4, 3+3 90,	13H,		13H, 17H 1.4,			13H,
	70% Fuel/Spark/30% Fuel, 0.4 Phi Tot			3+3 90,						
	50% Fuel/Spark/50% Fuel, 0.6Phi Tot	FSF 70 generally a better compromise								
	60% Fuel/Spark/40% Fuel, 0.6Phi Tot									
	70% Fuel/Spark/30% Fuel, 0.6Phi Tot			13H, 17H 1.4, 3+3 90,			13H, 17H 1.4,			
	80% Fuel/Spark/20% Fuel, 0.6Phi Tot									
	50% Fuel/50% Fuel/Spark, 0.4Phi Tot			13H, 3+3 90,						
	70% Fuel/30% Fuel/Spark, 0.4Phi Tot	17H 1.4, 3+3 90,		13H, 17H 1.4, 3+3 90,			13H,			
	80% Fuel/20% Fuel/Spark, 0.4 Phi Tot			3+3 90,						
	50% Fuel/50% Fuel/Spark, 0.6Phi Tot									
	70% Fuel/30% Fuel/Spark, 0.6Phi Tot			3+3 90,						
	80% Fuel/20% Fuel/Spark, 0.6Phi Tot			13H,						

Figure A.3: Injectors/Combustion Chamber/Tests Conducted, part 3.

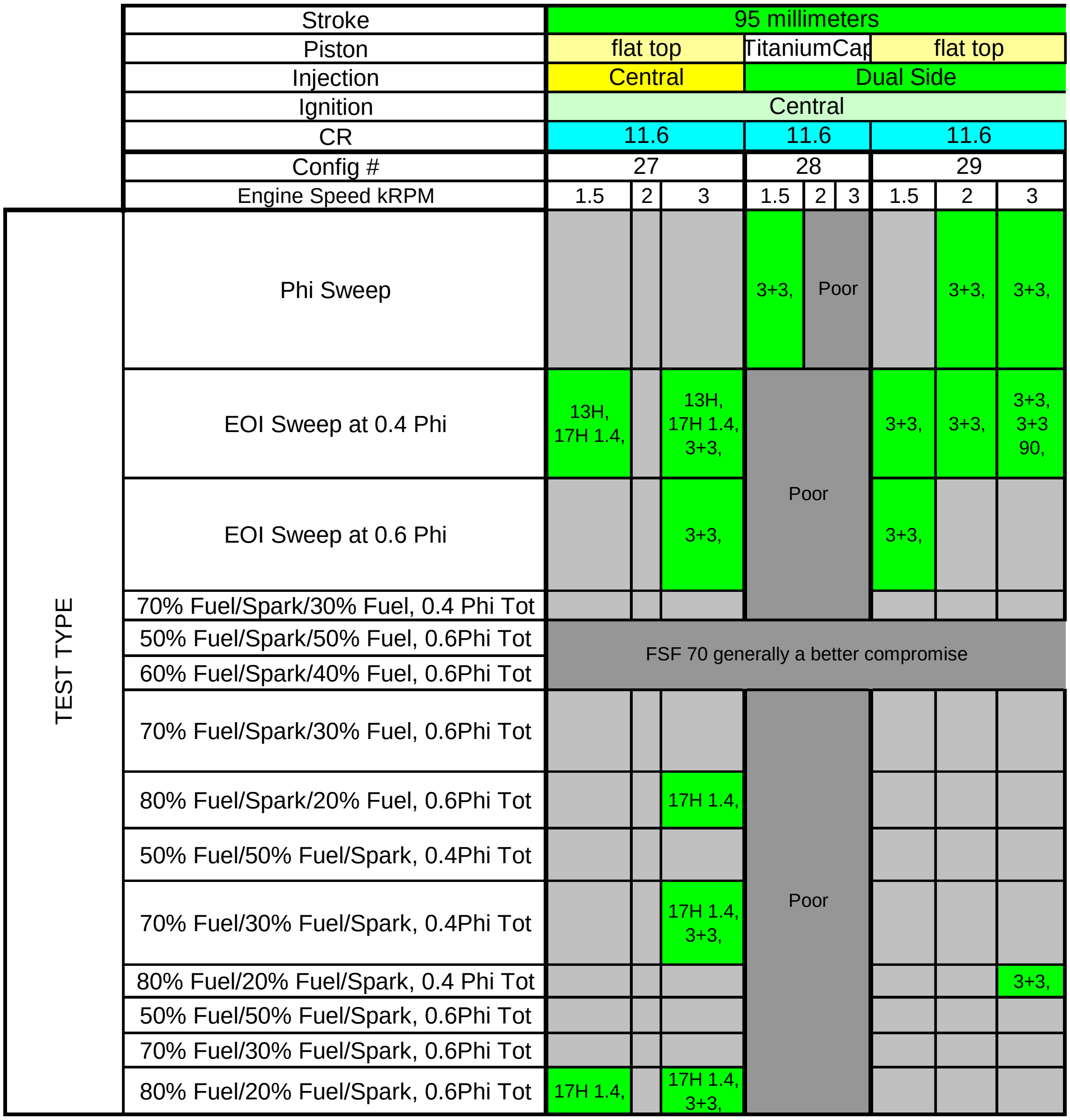

		27			28			29		
	Stroke	95 millimeters								
	Piston	flat top			TitaniumCap			flat top		
	Injection	Central			Dual Side					
	Ignition	Central								
	CR	11.6			11.6			11.6		
	Config #	27			28			29		
	Engine Speed kRPM	1.5	2	3	1.5	2	3	1.5	2	3
TEST TYPE	Phi Sweep				3+3,	Poor			3+3,	3+3,
	EOI Sweep at 0.4 Phi	13H, 17H 1.4,		13H, 17H 1.4, 3+3,	Poor			3+3,	3+3,	3+3, 3+3 90,
	EOI Sweep at 0.6 Phi			3+3,				3+3,		
	70% Fuel/Spark/30% Fuel, 0.4 Phi Tot									
	50% Fuel/Spark/50% Fuel, 0.6Phi Tot	FSF 70 generally a better compromise								
	60% Fuel/Spark/40% Fuel, 0.6Phi Tot									
	70% Fuel/Spark/30% Fuel, 0.6Phi Tot				Poor					
	80% Fuel/Spark/20% Fuel, 0.6Phi Tot			17H 1.4,						
	50% Fuel/50% Fuel/Spark, 0.4Phi Tot									
	70% Fuel/30% Fuel/Spark, 0.4Phi Tot			17H 1.4, 3+3,						
	80% Fuel/20% Fuel/Spark, 0.4 Phi Tot									3+3,
	50% Fuel/50% Fuel/Spark, 0.6Phi Tot									
	70% Fuel/30% Fuel/Spark, 0.6Phi Tot									
	80% Fuel/20% Fuel/Spark, 0.6Phi Tot	17H 1.4,		17H 1.4, 3+3,						

Figure A.3: Injectors/Combustion Chamber/Tests Conducted, part 3.

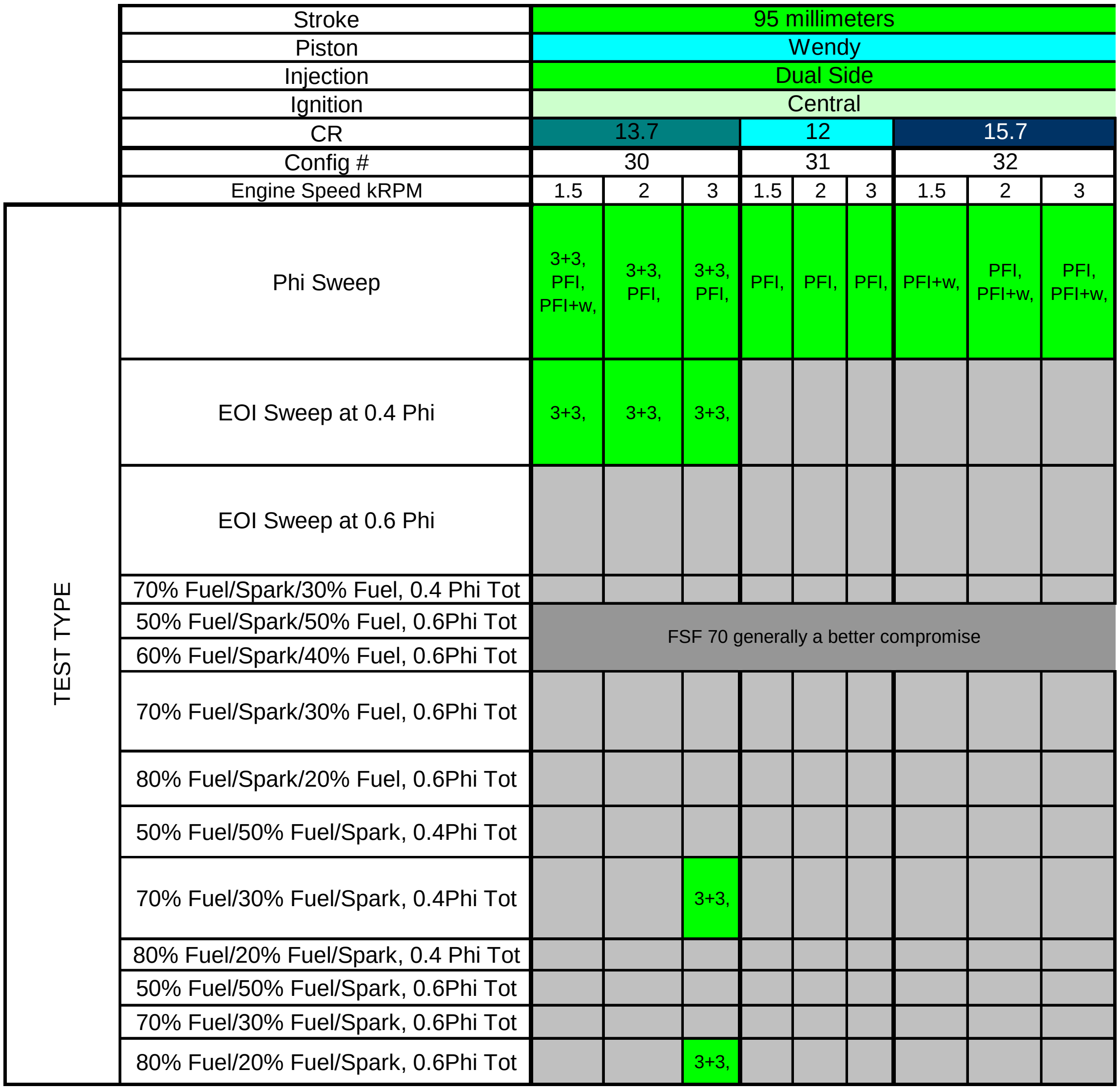

	Stroke	95 millimeters								
	Piston	Wendy								
	Injection	Dual Side								
	Ignition	Central								
	CR	13.7			12			15.7		
	Config #	30			31			32		
	Engine Speed kRPM	1.5	2	3	1.5	2	3	1.5	2	3
TEST TYPE	Phi Sweep	3+3, PFI, PFI+w,	3+3, PFI,	3+3, PFI,	PFI,	PFI,	PFI,	PFI+w,	PFI, PFI+w,	PFI, PFI+w,
	EOI Sweep at 0.4 Phi	3+3,	3+3,	3+3,						
	EOI Sweep at 0.6 Phi									
	70% Fuel/Spark/30% Fuel, 0.4 Phi Tot									
	50% Fuel/Spark/50% Fuel, 0.6Phi Tot	FSF 70 generally a better compromise								
	60% Fuel/Spark/40% Fuel, 0.6Phi Tot									
	70% Fuel/Spark/30% Fuel, 0.6Phi Tot									
	80% Fuel/Spark/20% Fuel, 0.6Phi Tot									
	50% Fuel/50% Fuel/Spark, 0.4Phi Tot									
	70% Fuel/30% Fuel/Spark, 0.4Phi Tot			3+3,						
	80% Fuel/20% Fuel/Spark, 0.4 Phi Tot									
	50% Fuel/50% Fuel/Spark, 0.6Phi Tot									
	70% Fuel/30% Fuel/Spark, 0.6Phi Tot									
	80% Fuel/20% Fuel/Spark, 0.6Phi Tot			3+3,						

Figure A.4: Injectors/Combustion Chamber/Tests Conducted, part 4.

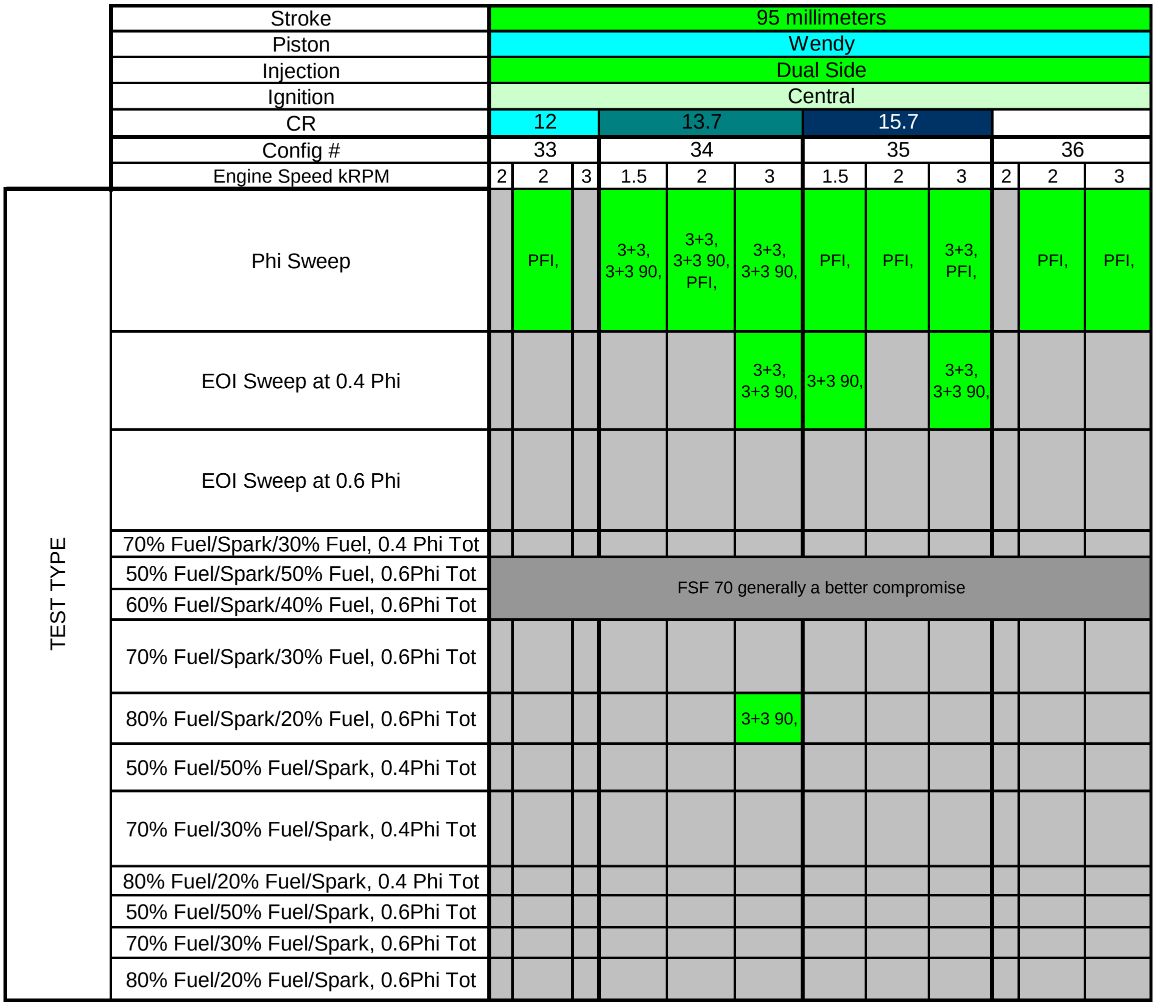

	Stroke	95 millimeters											
	Piston	Wendy											
	Injection	Dual Side											
	Ignition	Central											
	CR	12			13.7			15.7					
	Config #	33			34			35			36		
	Engine Speed kRPM	2	2	3	1.5	2	3	1.5	2	3	2	2	3
TEST TYPE	Phi Sweep		PFI,		3+3, 3+3 90,	3+3, 3+3 90, PFI,	3+3, 3+3 90,	PFI,	PFI,	3+3, PFI,		PFI,	PFI,
	EOI Sweep at 0.4 Phi						3+3, 3+3 90,	3+3 90,		3+3, 3+3 90,			
	EOI Sweep at 0.6 Phi												
	70% Fuel/Spark/30% Fuel, 0.4 Phi Tot												
	50% Fuel/Spark/50% Fuel, 0.6Phi Tot	FSF 70 generally a better compromise											
	60% Fuel/Spark/40% Fuel, 0.6Phi Tot												
	70% Fuel/Spark/30% Fuel, 0.6Phi Tot												
	80% Fuel/Spark/20% Fuel, 0.6Phi Tot						3+3 90,						
	50% Fuel/50% Fuel/Spark, 0.4Phi Tot												
	70% Fuel/30% Fuel/Spark, 0.4Phi Tot												
	80% Fuel/20% Fuel/Spark, 0.4 Phi Tot												
	50% Fuel/50% Fuel/Spark, 0.6Phi Tot												
	70% Fuel/30% Fuel/Spark, 0.6Phi Tot												
	80% Fuel/20% Fuel/Spark, 0.6Phi Tot												

Figure A.5: Injectors/Combustion Chamber/Tests Conducted, part 5.

Bibliography

[1] S. Verhelst and T. Wallner, "Hydrogen-Fueled Internal Combustion Engines," *Progress in Energy and Combustion Science*, 2009.

[2] A. Rousseau, T. Wallner, and H. Lohse-busch, "Prospects on Fuel Economy Improvements for Hydrogen Powered Vehicles," *SAE*, no. 2008–01–2378, 2008.

[3] M. F. Rosati and P. G. Aleiferis, "Hydrogen SI and HCCI Combustion in a Direct-Injection Optical Engine," *SAE*, no. 2009–01–1921, 2009.

[4] A. Lanz, J. Heffel, and C. Messer, "No Title," *Hydrogen Fuel Cell Engines and Related Technologies*, 2001.

[5] C. K. Law, *Combustion Physics*. Cambridge University Press, 2006, p. 7.

[6] T. Kondo, S. Lio, and H. Masaru, "A Study on the Mechanism of Backfire in External Mixture Formation Hydrogen Engines," *SAE*, no. 971704, 1997.

[7] X. Tang, D. M. Kabat, R. J. Natkin, W. F. Stockhausen, and F. M. Co, "Ford P2000 Hydrogen Engine Dynamometer Development Reprinted From : SI Combustion and Flow Diagnostics," *SAE*, no. 2002–01–0242, 2002.

[8] C. White, R. Steeper, and a Lutz, "The hydrogen-fueled internal combustion engine: a technical review," *International Journal of Hydrogen Energy*, vol. 31, no. 10, pp. 1292–1305, Aug. 2006.

[9] B. Lewis and G. Von Elbe, *Combustion, Flames and Explosions of Gases*, 3rd ed. Orlando: Academic Press, 1987.

[10] R. Owston, V. Magi, and J. Abraham, "Wall Interactions of Hydrogen Flames Compared with Hydrocarbon Flames," *SAE*, no. 2007–01–1466, 2007.

[11] M. K. Roy, N. Kawahara, E. Tomita, and T. Fujitani, "High-Pressure Hydrogen Jet and Combustion Characteristics in a Direct-Injection Hydrogen Engine .," *SAE*, no. 2011–01–2003, 2011.

[12] B. R. Petersen and J. B. Ghandhi, "Transient High-Pressure Hydrogen Jet Measurements," *SAE*, no. 2006–01–0652, 2006.

[13] B. R. Petersen, "Transient High-Pressure Hydrogen Jet Measurements," University of Wisconsin, 2006.

[14] T. Wallner, N. S. Matthias, and R. Scarcelli, "Influence of Injection Strategy in a High-Efficiency Hydrogen Direct Injection Engine," *SAE*, no. 2011–01–2001, 2011.

[15] T. Wallner, A. M. Nande, and J. D. Naber, "Study of Basic Injection Configurations using a Direct-Injection Hydrogen Research Engine ij Spark plug Exhaust valves," *SAE*, no. 2009–01–1418, 2009.

[16] N. S. Matthias, T. Wallner, and R. Scarcelli, "A Hydrogen Direct Injection Engine Concept that Exceeds U . S . DOE Light-Duty Efficiency Targets," *SAE*, no. 2012–01–0653, 2012.

[17] J. M. Kim, Y. T. Kim, J. T. Lee, and S. Y. Lee, "Performance Characteristics of Hydrogen Fueled Engine with the Direct Injection and Spark Ignition System," *SAE*, no. 952498, 1995.

[18] T. Wallner, A. M. Nande, and J. Naber, "Evaluation of Injector Location and Nozzle Design in a Direct-Injection Hydrogen," *SAE*, no. 2008–01–1785, 2008.

[19] V. Salazar and S. Kaiser, "Interaction of Intake-Induced Flow and Injection Jet in a Direct-Injection Hydrogen-Fueled Engine Measured by PIV," *SAE*, no. 2011–04–0673, 2011.

[20] V. M. Salazar, S. A. Kaiser, and F. Halter, "Optimizing Precision and Accuracy of Quantitative PLIF of Acetone as a Tracer for Hydrogen Fuel," *SAE*, no. 2009–01–1534, 2009.

[21] R. Scarcelli, T. Wallner, V. M. Salazar, and S. A. Kaiser, "Modeling and Experiments on Mixture Formation in a Hydrogen Direct-Injection Research Engine," 2009.

[22] V. Salazar and S. Kaiser, "Influence of the Flow Field on Flame Propagation in a Hydrogen-Fueled Internal Combustion Engine," *SAE*, no. 2011–24–0098, 2011.

[23] V. M. Salazar and S. A. Kaiser, "An Optical Study of Mixture Preparation in a Hydrogen-fueled Engine with Direct Injection Using Different Nozzle Designs," *SAE*, no. 2009–01–2682, 2009.

[24] R. Scarcelli, T. Wallner, V. M. Salazar, and S. A. Kaiser, "Modeling and Experiments on Mixture Formation in a Hydrogen Direct-Injection Research Engine," *SAE*, no. 2009–24–0083, 2009.

[25] R. Scarcelli, T. Wallner, N. Matthias, V. Salazar, and S. Kaiser, "Mixture Formation in Direct Injection Hydrogen Engines : CFD and Optical Analysis of Single- and Multi-Hole Nozzles," *SAE*, no. 2011–24–0096, 2011.

[26] A. M. Nande, T. Wallner, and J. Naber, "Influence of Water Injection on Performance and Emissions of a Direct-Injection Hydrogen Research Engine," *SAE*, no. 2008–01–2377, 2008.

[27] C. Bleechmore and S. Brewster, "Dilution Strategies for Load and NOx Management in a Hydrogen Fuelled Direct Injection Engine," *SAE*, no. 2007–01–4097, 2007.

[28] A. Rousseau, S. Pagerit, T. Wallner, and H. Lohse, "Comparison Between Fuel Cell and Hydrogen Engine Fuel Consumption," 2008.

[29] A. Welch, D. Mumford, S. Munshi, J. Holbery, B. Boyer, M. Younkins, and H. Jung, "Challenges in Developing Hydrogen Direct Injection Technology for Internal Combustion Engines," *SAE*, vol. 2008–01–23, no. 724, 2008.

[30] E. Pipitone, A. Beccari, and S. Beccari, "Reliable TDC position determination : a comparison of different thermodynamic methods through experimental data and Reliable TDC position determination : a comparison of different thermodynamic methods through experimental data and," *SAE*, no. 2008–36–0059, 2008.

[31] J. D. Stank, "Analysis of in-cylinder pressure transducer data quality utilizing a SIDI turbocharged engine," Michigan Technological University, 2011.

[32] K. Z. Mendera and A. Spyra, "Mass fraction burned analysis," *Journal of KONES Internal Combustion Engines*, no. 3, pp. 193–201, 2002.

[33] G. Smith, D. Golden, M. Frenklach, N. Moriarty, B. Eiteneer, M. Goldenberg, C. T. Bowman, R. Hanson, S. Song, W. Gardiner, V. Lissianski, and Z. Qin, "GRI-Mech 3.0," 1997. [Online]. Available: http://www.me.berkeley.edu/gri_mech/version30/text30.html. [Accessed: 04-Aug-2012].

[34] H. Blaxill, S. Reader, S. Mackay, and M. I. Gmbh, "Development of a Friction Optimized Engine," *SAE*, no. 2009–01–1052, 2009.

[35] V. Salazar and S. Kaiser, "Influence of the Flow Field on Flame Propagation in a Hydrogen-Fueled Internal Combustion Engine," *SAE*, no. 2011–24–0098, pp. 2376–2394, 2011.

[36] R. Scarcelli, T. Wallner, N. Matthias, V. Salazar, and S. Kaiser, "Numerical and Optical Evolution of Gaseous Jets in Direct Injection Hydrogen Engines," *SAE*, no. 2011–01–0675, 2011.

[37] C. M. White, "PIV and PLIF to Evaluate Mixture Formation in a Direct-Injection Hydrogen-Fuelled Engine," *SAE*, no. 2008–01–1034, 2008.

[38] C. M. White, "A Qualitative Evaluation of Mixture Formation in a Direct-Injection Hydrogen-Fuelled Engine," *SAE*, no. 2007–01–1467, 2007.